AMICO galaxy clusters in KiDS-1000: Splashback radius from weak lensing and cluster-galaxy correlation function

G. F. Lesci[1,2], C. Giocoli[1,2,3], F. Marulli[1,2,3], M. Romanello[1,2], L. Moscardini[1,2,3], M. Sereno[2,3], M. Maturi[4,5],
M. Radovich[6], G. Castignani[2], H. Hildebrandt[8], L. Ingoglia[1,7], and E. Puddu[9]

[1] Dipartimento di Fisica e Astronomia "Augusto Righi" - Alma Mater Studiorum Università di Bologna, via Piero Gobetti 93/2,
    I-40129 Bologna, Italy
[2] INAF - Osservatorio di Astrofisica e Scienza dello Spazio di Bologna, via Piero Gobetti 93/3, I-40129 Bologna, Italy
[3] INFN - Sezione di Bologna, viale Berti Pichat 6/2, I-40127 Bologna, Italy
[4] Zentrum für Astronomie, Universität Heidelberg, Philosophenweg 12, D-69120 Heidelberg, Germany
[5] ITP, Universität Heidelberg, Philosophenweg 16, 69120 Heidelberg, Germany
[6] INAF - Osservatorio Astronomico di Padova, vicolo dell'Osservatorio 5, I-35122 Padova, Italy
[7] INAF - Istituto di Radioastronomia, Via Piero Gobetti 101, 40129 Bologna, Italy
[8] Ruhr University Bochum, Faculty of Physics and Astronomy, Astronomical Institute (AIRUB), German Centre for Cosmological
    Lensing, 44780 Bochum, Germany
[9] INAF - Osservatorio Astronomico di Capodimonte, Salita Moiariello 16, Napoli 80131, Italy

Received –; accepted –

ABSTRACT

Aims. We present the splashback radius analysis of the Adaptive Matched Identifier of Clustered Objects (AMICO) galaxy cluster sample in the fourth data release of the Kilo Degree Survey (KiDS). The sample contains 9049 rich galaxy clusters within $z \in [0.1, 0.8]$, with shear measurements available for 8730 of them.
Methods. We measure and model the stacked reduced shear, g_t, and the cluster-galaxy correlation function, w_{cg}, in bins of observed intrinsic richness, λ^*, and redshift, z. Building on the methods employed in recent cosmological analyses, we model the average splashback radius, r_{sp}, of the underlying dark matter halo distribution, accounting for the known systematic uncertainties affecting measurements and theoretical models.
Results. By modelling g_t and w_{cg} separately, in the cluster-centric radial range $R \in [0.4, 5]\ h^{-1}$Mpc, we constrain r_{sp}, the mass accretion rate, Γ, and the relation between $\mathcal{R}_{sp} \equiv r_{sp}/r_{200m}$ and the peak height, ν_{200m}, over the mass range $M_{200m} \in [0.4, 20]\ 10^{14}h^{-1}M_{\odot}$. The two probes provide consistent results that also agree with Λ-cold dark matter model predictions. Our $\mathcal{R}_{sp}$ constraints are consistent with those from previous observations. For g_t and w_{cg}, we achieve a precision of 14% and 10% per cluster stack, respectively. The higher precision of w_{cg}, enabled by its combination with weak-lensing constraints on the mass-richness relation, highlights the complementarity of lensing and clustering in measuring r_{sp} and constraining the properties of the infalling material region.

Key words. clusters – Galaxies: clusters: general – Galaxies: kinematics and dynamics – Cosmology: observations

1. Introduction

The mass profiles of dark matter haloes have been extensively investigated using *N*-body simulations (see e.g. Einasto 1965; Navarro, Frenk, & White 1997; Baltz, Marshall, & Oguri 2009), establishing a robust theoretical foundation for interpreting galaxy cluster observations. Precise measurements of the inner and virialised regions of clusters not only support cosmological analyses based on cluster statistics (Planck Collaboration XXIV 2016; Costanzi et al. 2019; Marulli et al. 2021; Romanello et al. 2024; Seppi et al. 2024; Ghirardini et al. 2024; Lesci et al. 2025), but also enable tests of gravity theories (Pizzuti et al. 2017; Cardone et al. 2021; Mitchell et al. 2021; Rosselli et al. 2023) and constraints on dark matter self-interactions (Peter et al. 2013; Robertson et al. 2019; Eckert et al. 2022; Bhattacharyya et al. 2022; Despali et al. 2025). In addition, measurements in the outer halo regime, commonly referred to as the two-halo region and dominant beyond 2–5 Mpc from clus-

ter centres (Tinker et al. 2005), offer a complementary route to constrain cosmological parameters and cluster masses (Covone et al. 2014; Sereno et al. 2018; Giocoli et al. 2021; Ingoglia et al. 2022; Eltvedt et al. 2024).

In the transition between the virialised region and the two-halo regime, a sharp steepening in the density profile is expected. This feature, located in the proximity of the *splashback radius*, r_{sp}, was initially predicted from analytical models of spherical secondary collapse by Fillmore & Goldreich (1984) and Bertschinger (1985), and then robustly identified in dark matter simulations (Diemer & Kravtsov 2014; Adhikari et al. 2014; More et al. 2015). The splashback radius marks the apocentre of the first orbit of recently accreted material and, in turn, it strongly depends on the mass accretion rate, Γ. At fixed mass, haloes with higher Γ exhibit smaller r_{sp} due to the deepening of the gravitational potential well during the orbit of infalling material. More massive subhaloes also tend to have a smaller orbit apocentre than the less massive ones, an effect attributed to dynamical friction (Diemer et al. 2017; Chang et al. 2018), which slows down satellites by dissipating kinetic energy, thereby bringing

Send offprint requests to: G. F. Lesci
e-mail: `giorgio.lesci2@unibo.it`

them deeper into the potential well. Unlike halo concentration, the location of r_{sp} is more sensitive to recent accretion (within the last crossing time) than to the entire assembly history (Shin & Diemer 2023). However, the depth and width of the associated density steepening are strongly influenced by the full halo assembly history, providing complementary information on the location of the splashback radius (Yu et al. 2025).

As r_{sp} delineates a boundary between first-infalling matter and matter that has completed at least one passage through the central region of the halo, the mass enclosed within r_{sp} comprises all material accreted by a given redshift, z. Therefore, this mass definition remains unaffected by pseudo-evolution (More et al. 2015) and can potentially lead to the derivation of universal halo mass function models (Diemer 2020b; Ryu & Lee 2021, 2022). In fact, recent studies highlight the distinction between orbiting and infalling particles as the key factor in the definition of a halo (see Vladimir et al. 2025, and references therein). Furthermore, r_{sp} has been shown to correlate with fundamental cosmological parameters, such as the matter density parameter at $z = 0$, Ω_m, and the square root of the mass variance on a scale of 8 h^{-1}Mpc at $z = 0$, σ_8 (Diemer et al. 2017; Haggar et al. 2024; Mpetha et al. 2024).

It is critical to note that the physical origin of r_{sp} lies in the dynamics of halo particles. Diemer (2017, 2020a) showed that the radius of the steepest slope, which is directly observable in the mass density profiles, is a scattered proxy of r_{sp} (see also Sun et al. 2025). This occurs because the apocentres are distributed across a wide radial range due to non-spherical halo shapes, complex accretion histories, and gravitational interactions with neighbouring haloes. Alternative halo boundary definitions have been proposed in the literature, such as the depletion radius (Fong & Han 2021; Zhou & Han 2023), which is about 2 times larger than r_{sp} and corresponds to the scale above which the matter density decreases with time. Pizzardo et al. (2024) demonstrated that the inflection point in the radial velocity profile of cluster galaxies agrees with r_{sp} within 1σ, establishing an additional connection between the splashback radius and the inner boundary of the cluster infall region. García et al. (2023) and Salazar et al. (2025) showed that a clear truncation radius is apparent in the halo–matter correlation function, when particles are classified as bound or infalling based on their phase-space trajectories and accretion history.

In this work, following standard nomenclature in the literature, we define the radius of steepest slope as the splashback radius. We constrained the splashback radii of the galaxy clusters detected with the Adaptive Matched Identifier of Clustered Objects (AMICO, Bellagamba et al. 2018; Maturi et al. 2019) in the fourth data release of the Kilo Degree Survey (KiDS-1000, Kuijken et al. 2019). The cluster sample used in this work comprises 8730 rich clusters, spanning a total mass range of $M_{200m} \in [0.4, 20]\ 10^{14}h^{-1}M_\odot$ and extending up to a redshift $z = 0.8$. We measured and modelled the stacked weak-lensing profiles and cluster-galaxy correlation function of ensembles of clusters, constraining the relation between the peak height, ν_{200m}, and the normalised splashback radius, $\mathcal{R}_{sp} \equiv r_{sp}/r_{200m}$, where r_{200m} is the radius enclosing a mass M_{200m}, such that the corresponding mean density is 200 times the mean density of the Universe at the halo redshift. We also derived the mass accretion rate as a function of mass and redshift. Our results are competitive, in terms of statistical uncertainties, with those from previous analyses of observed cluster samples (More et al. 2016; Baxter et al. 2017; Umetsu & Diemer 2017; Chang et al. 2018; Contigiani et al. 2019; Zürcher & More 2019; Shin et al. 2019; Murata et al. 2020; Bianconi et al. 2021; Shin et al. 2021; Rana et al.

2023; Joshi et al. 2025). Compared to the analogous analysis by Giocoli et al. (2024), based on AMICO detections in the third data release of KiDS (KiDS-DR3, de Jong et al. 2017), we employed more conservative galaxy and cluster selections, and used a more extensive modelling of systematic uncertainties. Nevertheless, we achieve a comparable precision on the splashback radius to Giocoli et al. (2024), since the survey effective area is more than doubled compared to KiDS-DR3, and the cluster sample extends up to larger redshifts.

The paper is organised as follows. In Sect. 2 we present the galaxy cluster and shear samples, while in Sect. 3 the measurements of stacked weak-lensing profiles and cluster-galaxy correlation function are presented. In Sect. 4, we outline the theoretical framework, likelihood function, and prior distributions used in this work. We present our results in Sect. 5 and our conclusions in Sect. 6.

In this work, we adopted a concordance flat Λ cold dark matter (ΛCDM) cosmological model. The base 10 logarithm is referred to as log, while ln represents the natural logarithm. The statistical analyses presented in this paper were performed using the `CosmoBolognaLib`[1] (CBL, Marulli et al. 2016), a set of *free software* C++/Python numerical libraries for cosmological calculations. The linear matter power spectrum is computed with `CAMB`[2] (Lewis & Challinor 2011).

2. Data set

In our analysis we used KiDS-1000 data (Kuijken et al. 2019), which are based on imaging obtained with the OmegaCAM wide-field camera (Kuijken 2011), operating on the VLT Survey Telescope (VST, Capaccioli & Schipani 2011). The KiDS-1000 release comprises 1006 square-degree tiles, each spanning roughly 1 deg^2. It includes 2 arcsecond aperture photometry in the *u*, *g*, *r*, and *i* optical bands, with 5σ depth limits of 24.23, 25.12, 25.02, and 23.68 magnitudes, respectively. Complementary near-infrared photometry in the *Z*, *Y*, *J*, *H*, and K_s bands is also provided by the VISTA Kilo-degree INfrared Galaxy survey (VIKING, Edge et al. 2013; Sutherland et al. 2015), which fully overlaps the KiDS footprint.

The galaxy cluster sample analysed in this work originates from the AMICO KiDS-1000 catalogue (Maturi et al. 2025, M25 hereafter), constructed by applying the AMICO algorithm (Bellagamba et al. 2018; Maturi et al. 2019) to KiDS-1000 photometric data. AMICO uses an optimal matched filter and is one of the official cluster-finding tools of the *Euclid* mission (Euclid Collaboration: Adam et al. 2019). The catalogue excludes regions affected by image artefacts and photometric issues, resulting in a clean survey area of 839 deg^2, with cluster detections up to $z = 0.9$. Following Lesci et al. (2025, L25 hereafter), we restricted our analysis to clusters with S/N > 3.5 and redshifts $z \in [0.1, 0.8]$, yielding 22 396 detections. Additional cuts in the cluster mass proxy, namely the intrinsic richness λ^* (see M25), yield a final cluster sample of 8730 objects, as discussed in Sect. 3. These selections optimise the trade-off between fit quality and sample size (L25). Cluster redshifts have been corrected for the bias identified by M25, based on a comparison with spectroscopic redshifts available within the KiDS data set (collectively referred to as KiDZ, van den Busch et al. 2020, 2022). These spectroscopic redshifts come from the Galaxy and Mass Assembly survey data release 4 (GAMA-DR4, Driver et al. 2011; Liske et al. 2015; Driver et al. 2022), the Sloan Digital Sky
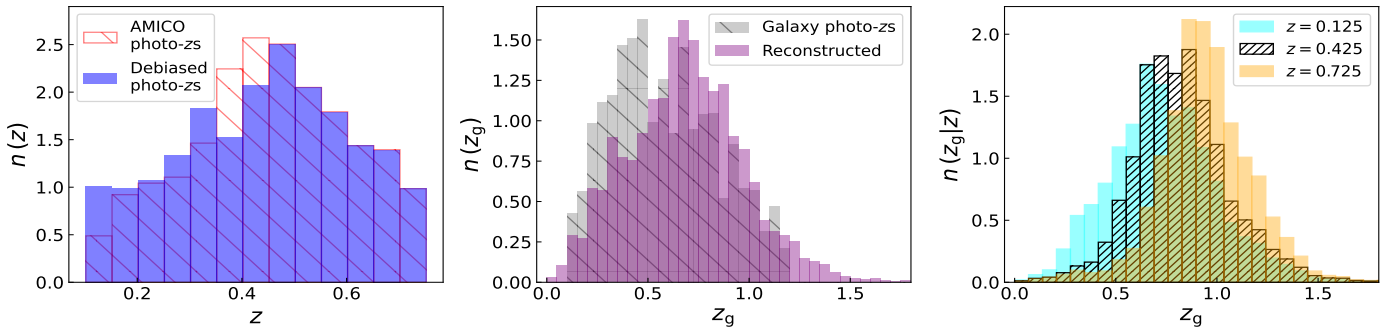
---

[1] https://gitlab.com/federicomarulli/CosmoBolognaLib/
[2] https://camb.info/

Fig. 1. Left panel: Cluster photo-z distributions as measured by AMICO (hatched red) and unbiased using a reference spectroscopic sample (blue). Middle panel: Observed photo-z (hatched grey) and SOM-reconstructed (purple) redshift distributions of the full galaxy sample. Right panel: examples of SOM-reconstructed background galaxy redshift distributions, given a cluster redshift of $z = 0.125$ (cyan), $z = 0.425$ (hatched black), $z = 0.725$ (orange), derived by using the background selections by L25.

Survey (SDSS, Alam et al. 2015), and the 2-degree Field Lensing Survey (2dFLens, Blake et al. 2016). Each AMICO cluster has been assigned a bias-corrected redshift, with a resulting precision of $\sigma_z/(1 + z) = 0.014$. The left panel of Fig. 1 displays the comparison of measured and debiased AMICO cluster redshift distributions.

As in Kuijken et al. (2019), M25 employed the `Bayesian Photometric Redshift` (BPZ, Benítez 2000) code to estimate galaxy photometric redshifts for cluster detection. The prior on redshift probabilities used in Kuijken et al. (2019) was optimised for the weak-lensing analysis, reducing uncertainties and catastrophic outliers for faint, high-redshift galaxies. However, it introduced a significant bias for bright, low-redshift galaxies, which are important for cluster detection. For this reason, M25 adopted instead the redshift prior used in the KiDS-DR3 analysis (de Jong et al. 2017). This choice results in a galaxy photometric redshift (photo-z) uncertainty of $\sigma_{z,g}/(1 + z) = 0.074$ for galaxies with $r < 23$, consistent with the findings of Kuijken et al. (2019). In the present work, we used photometric redshifts derived following this approach.

To measure the weak-lensing profiles of AMICO galaxy clusters, we utilised the KiDS-1000 gold shear catalogue (Wright et al. 2020; Hildebrandt et al. 2021; Giblin et al. 2021). This data set contains approximately 21 million galaxies across an effective area of 777 deg², with a weighted effective number density of $n_{\text{eff}}^{\text{gold}} = 6.17$ arcmin^{-2}. Shape measurements are based on the deep KiDS r-band imaging, and shear estimates are derived by employing the *lensfit* algorithm (Miller et al. 2007; Fenech Conti et al. 2017). Following Hildebrandt et al. (2021), we considere galaxies having redshift in the range $z_g \in [0.1, 1.2]$. We used the same galaxy catalogue to measure the cluster-galaxy correlation function (Sect. 3.2). To ensure spatial matching, we restricted the cluster sample to the footprint of the galaxy sample, since the latter has a smaller effective area. For correlation function measurements, we also applied the $r < 24$ magnitude cut, corresponding to the depth of the shallowest survey tile, to ensure homogeneity of the angular galaxy distribution (following M25).

Following Hildebrandt et al. (2021), we reconstructed galaxy redshift distributions using self-organising maps (SOM; Kohonen 1982; Wright et al. 2020). We did not use the galaxy redshift distributions from Hildebrandt et al. (2021), as our analysis adopts a different photo-z estimation method and a different binning strategy. Instead, we applied SOM to the spectroscopic sample from van den Busch et al. (2022) and extended by Wright et al. (2024), comprising 93 224 galaxies. While M25

used a different method to estimate the unbiased cluster redshift distribution compared to the SOM-based approach we applied to galaxies, we do not expect this to introduce systematics. Indeed, as discussed in the following, our analysis accounts for the statistical uncertainties of both the galaxy and cluster redshift distributions. We employed the SOM algorithm introduced by Wright et al. (2020) and subsequently implemented by Hildebrandt et al. (2021) for KiDS-1000 redshift distribution calibration, based on the `kohonen` code (Wehrens & Buydens 2007; Wehrens & Kruisselbrink 2018). Following Wright et al. (2020) and L25, we provided the SOM algorithm with photometric data from all 9 KiDS and VIKING bands, including their full colour space combinations. The SOM architecture employs a toroidal topology with a 50×50 hexagonal grid. The middle panel in Fig. 1 shows the observed distribution of the full galaxy sample as a function of galaxy redshift, z_g, along with the corresponding SOM-reconstructed distribution. The latter was employed in the cluster-galaxy correlation function modelling. The right panel of Fig. 1 displays three representative SOM-reconstructed background galaxy redshift distributions, each conditioned on a different cluster redshift. These distributions are measured in cluster redshift bins having a width of $\delta z = 0.05$ and spanning the full sample range, based on a combination of colour and photo-z background selections (for details, we refer to L25). We used these reconstructed background redshift distributions in the weak-lensing modelling.

3. Measurements

In this section, we present the measurements of stacked cluster lensing (Sect. 3.1) and cluster-galaxy correlation function (Sect. 3.2). The lensing measurement pipeline follows that of L25, who carried out the mass calibration of the cluster sample analysed in this work. The properties of the cluster subsamples are reported in Table 1. As shown in Fig. 2 of L25, these cluster subsamples have a purity ranging from 97% to 100%. Consistent with L25, for all profile measurements we adopted a flat ΛCDM cosmology with a Hubble constant of $H_0 = 70$ km s^{-1} Mpc^{-1} and $\Omega_m = 0.3$. Throughout this paper, we considered different Ω_m values to model our measurements. For the mass probe measurements considered in this work, cosmological dependence arises solely from the conversion to cluster-centric physical distances. As discussed in Sect. 4.4, we modelled the geometric distortions introduced by these assumptions.

Table 1. Properties of the cluster subsamples and main results.

z_{ob} range	λ^*_{ob} range	N	Median z_{ob}	Median λ^*_{ob}	$\langle M^{g_t}_{200m} \rangle$	$\langle r^{g_t}_{sp} \rangle$	$\langle r^{w_{cg}}_{sp} \rangle$	$\langle \mathcal{R}^{g_t}_{sp} \rangle$	$\langle \mathcal{R}^{w_{cg}}_{sp} \rangle$	$\langle \Gamma^{g_t} \rangle$	$\langle \Gamma^{w_{cg}} \rangle$
[0.10, 0.30)	[20, 40)	1411	0.24	25	$0.70^{+0.07}_{-0.06}$	$0.98^{+0.13}_{-0.13}$	$0.88^{+0.09}_{-0.07}$	$1.08^{+0.15}_{-0.14}$	$0.97^{+0.09}_{-0.09}$	$2.08^{+1.11}_{-0.90}$	$2.97^{+0.97}_{-0.77}$
[0.10, 0.30)	[40, 65)	255	0.25	46	$1.96^{+0.11}_{-0.12}$	$1.36^{+0.20}_{-0.18}$	$1.22^{+0.12}_{-0.09}$	$1.06^{+0.15}_{-0.13}$	$0.96^{+0.09}_{-0.09}$	$2.20^{+1.16}_{-0.93}$	$3.08^{+0.98}_{-0.79}$
[0.10, 0.30)	[65, 210]	47	0.25	78	$4.63^{+0.36}_{-0.37}$	$1.79^{+0.28}_{-0.25}$	$1.59^{+0.16}_{-0.12}$	$1.04^{+0.15}_{-0.13}$	$0.94^{+0.09}_{-0.09}$	$2.34^{+1.22}_{-0.97}$	$3.27^{+1.04}_{-0.83}$
[0.30, 0.45)	[25, 40)	1536	0.38	30	$0.83^{+0.07}_{-0.06}$	$0.93^{+0.14}_{-0.12}$	$0.84^{+0.08}_{-0.06}$	$1.08^{+0.15}_{-0.14}$	$0.99^{+0.10}_{-0.09}$	$2.30^{+1.19}_{-0.95}$	$3.11^{+0.99}_{-0.79}$
[0.30, 0.45)	[40, 65)	525	0.38	46	$1.82^{+0.10}_{-0.10}$	$1.19^{+0.18}_{-0.16}$	$1.08^{+0.10}_{-0.08}$	$1.07^{+0.16}_{-0.14}$	$0.97^{+0.10}_{-0.09}$	$2.41^{+1.23}_{-0.99}$	$3.22^{+1.04}_{-0.83}$
[0.30, 0.45)	[65, 210]	90	0.38	76	$4.23^{+0.32}_{-0.31}$	$1.54^{+0.24}_{-0.21}$	$1.39^{+0.14}_{-0.11}$	$1.05^{+0.16}_{-0.14}$	$0.95^{+0.10}_{-0.09}$	$2.57^{+1.30}_{-1.03}$	$3.44^{+1.13}_{-0.86}$
[0.45, 0.80]	[30, 45)	3616	0.64	35	$0.98^{+0.09}_{-0.08}$	$0.83^{+0.13}_{-0.11}$	$0.77^{+0.07}_{-0.06}$	$1.08^{+0.16}_{-0.14}$	$0.99^{+0.10}_{-0.10}$	$2.75^{+1.39}_{-1.05}$	$3.55^{+1.18}_{-0.89}$
[0.45, 0.80]	[45, 60)	930	0.63	50	$1.76^{+0.13}_{-0.14}$	$1.00^{+0.15}_{-0.14}$	$0.92^{+0.09}_{-0.07}$	$1.07^{+0.16}_{-0.14}$	$0.98^{+0.10}_{-0.10}$	$2.84^{+1.43}_{-1.09}$	$3.66^{+1.24}_{-0.91}$
[0.45, 0.80]	[60, 210]	320	0.61	68	$3.22^{+0.27}_{-0.27}$	$1.20^{+0.19}_{-0.17}$	$1.10^{+0.11}_{-0.09}$	$1.05^{+0.16}_{-0.14}$	$0.96^{+0.10}_{-0.09}$	$2.93^{+1.49}_{-1.12}$	$3.82^{+1.30}_{-0.96}$

Notes. The bins of observed cluster photo-z, z_{ob}, and intrinsic richness, λ^*_{ob}, are shown in the first and second columns, respectively. The third column lists the number of clusters used for the measurements, while the fourth and fifth columns report the median cluster redshift and richness, respectively. In the subsequent columns, we show the posteriors on the mean mass, $\langle M^{g_t}_{200m} \rangle$ (in units of $10^{14} h^{-1} M_\odot$), splashback radius, $\langle r_{sp} \rangle$ (in h^{-1}Mpc), normalised splashback radius, $\langle \mathcal{R}_{sp} \rangle \equiv \langle r_{sp}/r_{200m} \rangle$, and mass accretion rate, $\langle \Gamma \rangle$. The latter is dimensionless (see Eq. 45). The g_t and w_{cg} superscripts represent the results from weak lensing and cluster-galaxy correlation function, respectively.

3.1. Stacked weak-lensing profiles

The tangential shear, γ_t, is related to the excess surface density, $\Delta\Sigma_t$, through the following relation (see e.g. Sheldon et al. 2004):

$$\Delta\Sigma_t(R) = \overline{\Sigma}(< R) - \Sigma(R) = \Sigma_{crit}\gamma_t(R), \tag{1}$$

where $\Sigma(R)$ denotes the surface mass density at radius R, $\overline{\Sigma}(< R)$ is its mean enclosed within the radius R, and Σ_{crit} is the critical surface density, which is expressed as (Bartelmann & Schneider 2001)

$$\Sigma_{crit} \equiv \frac{c^2}{4\pi G} \frac{D_s}{D_l D_{ls}}, \tag{2}$$

where c is the speed of light, G is Newton's gravitational constant, while D_s, D_l, and D_{ls} are the observer-source, observer-lens, and lens-source angular diameter distances, respectively.

The weak-lensing observable linked to galaxy ellipticities is the reduced shear, namely $g = \gamma/(1 - \kappa)$, where $\kappa \equiv \Sigma/\Sigma_{crit}$ is the convergence (Schneider & Seitz 1995). We estimated the reduced tangential shear profile, g_t, of a cluster labelled as k as (see e.g. Viola et al. 2015):

$$g_{t,k}(R_j) = \left(\frac{\sum_{i \in j} w_i e_{t,i}}{\sum_{i \in j} w_i} \right) \frac{1}{1 + \mathcal{M}_j}, \tag{3}$$

where $e_{t,i}$ is the tangential component of the ellipticity of the ith background galaxy, j is the radial annulus index, with an associated average projected radius R_j, corresponding to the central value of the radial bin. The impact of this radial point definition on our results is expected to be negligible. Indeed, L25 demonstrated that for our sample, alternative estimates of the effective radius differ from R_j by only 0.1%. In addition, w_i is the statistical weight assigned to the measure of the source ellipticity of the ith background galaxy (Sheldon et al. 2004), while $\mathcal{M}_j$ denotes the average multiplicative shear bias, defined as

$$\mathcal{M}_j = \frac{\sum_{i \in j} w_i m_i}{\sum_{i \in j} w_i}, \tag{4}$$

where m_i is the multiplicative shear bias of the ith background galaxy. Following L25, for each background source we draw a value of m from a uniform distribution in the range $[-2\sigma_m, 2\sigma_m]$, where $\sigma_m = 0.02$ corresponds to the largest 1σ interval of the m distributions obtained by Giblin et al. (2021). We used this approximation because the m estimates by Giblin et al. (2021) were derived from redshift distributions that do not correspond to those considered in this work. The statistical uncertainty on m, σ_m, is propagated into the final results by including it in the covariance matrix (see Sect. 4.6). We neglected the shear additive bias term, because Giblin et al. (2021) constrained it to be 10^{-4}, which is an order of magnitude smaller than our stacked g_t uncertainties. The background galaxy samples are defined through the combination of the photo-z and colour selections defined in L25. In the modelling described in Sect. 4, we used the background redshift distributions reconstructed through SOM, as described in Sect. 2.

The stacked reduced shear profile in the pth bin of observed intrinsic richness, $\Delta\lambda^*_{ob,p}$, and in the qth bin of observed cluster redshift, $\Delta z_{ob,q}$, is expressed as

$$g_t(R_j, \Delta\lambda^*_{ob,p}, \Delta z_{ob,q}) = \frac{\sum_{k \in \Delta\lambda^*_{ob,p}, \Delta z_{ob,q}} W_{k,j}\, g_{t,k}(R_j)}{\sum_{k \in \Delta\lambda^*_{ob,p}, \Delta z_{ob,q}} W_{k,j}}, \tag{5}$$

where $g_{t,k}$ is given by Eq. (3), k runs over all clusters falling in the bins of λ^* and z, while $W_{k,j}$ is the total weight for the jth radial bin of the kth cluster, estimated as

$$W_{k,j} = \sum_{i \in j} w_i, \tag{6}$$

where i runs over the background galaxies in the jth radial bin. We used the same λ^* and z bins as L25, shown in Table 1. This λ^* and z selection yields a sample of 9049 clusters, which reduce to 8730 due to the smaller area covered by the shear sample compared to the cluster sample (see Sect. 2). We adopted the same minimum cluster-centric projected distance of 400 h^{-1}kpc as L25, but extended the maximum radius to 5 h^{-1}Mpc in order to include measurements of the infalling region of galaxy clusters. Ten logarithmically spaced radial bins are used.

The bootstrap-estimated covariance matrix for each stacked $g_t(R)$ measurement derives from 10 000 resamplings of the cluster profiles within the stack. This covariance estimate incorporates the intrinsic scatter in the observable-mass and

concentration-mass relations, along with miscentring effects and the contribution from the large-scale structure, though it does not account for the covariance due to background galaxies shared between clusters. However, as demonstrated by McClintock et al. (2019), for Stage-III surveys such shared-source contributions remain subdominant to shape noise and large-scale structure effects. Finally, we neglected the covariance across different redshift and richness bins, as its impact has been shown to be negligible in Stage-III surveys (McClintock et al. 2019).

3.2. Cluster-galaxy correlation function

The projected cluster-galaxy correlation function, denoted as w_{cg}, in the pth bin of intrinsic richness, $\Delta\lambda^*_{ob,p}$, and in the qth bin of cluster redshift, $\Delta z_{ob,q}$, is measured using the Landy-Szalay estimator (Landy & Szalay 1993), expressed as follows:

$$w_{cg}(R_j, \Delta\lambda^*_{ob,p}, \Delta z_{ob,q}) = \frac{\mathcal{D}_c\mathcal{D}_g(R_j) - \mathcal{D}_c\mathcal{R}_g(R_j) - \mathcal{R}_c\mathcal{D}_g(R_j)}{\mathcal{R}_c\mathcal{R}_g(R_j)} + 1 .$$
(7)

Compared to the Davis-Peebles estimator (Davis & Peebles 1983), Eq. (7) reduces variance and edge effects. In Eq. (7), R_j is the central point of the jth radial annulus, while $\mathcal{D}_c\mathcal{D}_g(R_j)$, $\mathcal{D}_c\mathcal{R}_g(R_j)$, $\mathcal{R}_c\mathcal{D}_g(R_j)$, and $\mathcal{R}_c\mathcal{R}_g(R_j)$ are the normalised data cluster - data galaxy, data cluster - random galaxy, random cluster - data galaxy, random cluster - random galaxy pairs, respectively. In Eq. (7), we adopted the same R_j points used for weak-lensing measurements.

To measure w_{cg}, we used the complete KiDS-1000 gold shear catalogue, imposing the magnitude cut $r < 24$ (see Sect. 2). As this cut corresponds to the depth of the shallowest tile, it ensures a homogeneous angular galaxy distribution. Furthermore, in Eq. (7), for each cluster we include all galaxies at a projected separation R_j along the line of sight. As a result the w_{cg} estimator is independent of cluster membership modelling. The w_{cg} model is defined consistently with this approach (see Sect. 4.3).

We constructed random cluster and random galaxy samples 80 times larger than the observed ones. The extraction of random (R.A., Dec) pairs accounts for the KiDS survey angular mask. We assigned random cluster redshifts by reshuffling the observed mean redshifts, which were subsequently used to define cluster-centric radial bins. For the random galaxy sample, no redshift information is required since galaxy redshifts do not enter the w_{cg} estimator (Eq. 7). The adopted cluster λ^*, z, and R bins are those used for the weak-lensing measurements presented in Sect. 3.1. Jackknife resampling was used to estimate the covariance matrix, with KiDS tiles defining the resampling regions. As in Sect. 3.1, we neglected the correlation between λ^* and z bins.

4. Modelling

4.1. 3D model for individual haloes

This section presents the theoretical description of individual three-dimensional (3D) mass profiles. The models for g_t and w_{cg} are presented in Sects. 4.2 and 4.3, respectively, while the corresponding expected values for ensembles of clusters are detailed in Sect. 4.4. For single clusters, we characterised the 3D mass distribution using a Diemer & Kravtsov (2014, DK14) profile, commonly adopted to model observational data (Baxter et al. 2017; Rana et al. 2023; Giocoli et al. 2024; Joshi et al. 2025).

The corresponding excess 3D density profile is expressed as follows:

$$\Delta\rho(r) = \rho_s \exp\left\{ -\frac{2}{\alpha}\left[\left(\frac{r}{r_s}\right)^\alpha - 1\right]\right\} f_{trans} + \rho_{outer} ,$$
(8)

where

$$f_{trans} = \left[1 + \left(\frac{r}{r_t}\right)^\beta\right]^{-\frac{\gamma}{\beta}} ,$$
(9)

$$\rho_{outer} = \rho_m b_e \left(\frac{r}{5r_{200m}}\right)^{-s_e} .$$
(10)

Equation (8) an Einasto (1965) profile multiplied by the transition factor, f_{trans}. Here, the dependency of $\Delta\rho$ on M_{200m} and z is not explicitly shown for brevity. In Eq. (8), ρ_s is the characteristic density and r_s is the scale radius, expressed as $r_s = r_{200m}/c_{200m}$, where c_{200m} is the halo concentration. As detailed in Sect. 4.4, we modelled c_{200m} via a log-linear scaling relation with M_{200m} and redshift, with the amplitude empirically constrained by our data. For the inner slope of the Einasto profile, we assumed $\alpha = 0.155 + 0.0095\nu^2_{vir}$ (Gao et al. 2008). Here, $\nu^2_{vir} = \delta^2_c(z)/\sigma^2(M_{vir})$ represents the peak height of the virial halo mass, namely M_{vir}, while $\delta_c(z)$ is the linear theory critical overdensity required for spherical collapse divided by the growth factor, and $\sigma^2(M_{vir})$ is the mass variance. For the virial overdensity definition, we adopted the fitting function by Bryan & Norman (1998). To be consistent with the α definition by Gao et al. (2008), we converted M_{200m} into M_{vir} assuming a Navarro, Frenk, & White (1997, NFW) profile. Furthermore, we note that by treating c_{200m} as a free parameter, any possible systematic errors arising from the assumptions on α are mitigated.

The Einasto profile in Eq. (8) is multiplied by a transition factor, f_{trans} (defined in Eq. 9), which smoothly connects the inner halo component to the external large-scale term, namely ρ_{outer} (defined in Eq. 10). The transition factor depends on the truncation radius, $r_t = F_t r_{200m}$, where F_t is the truncation factor, on β, defining the sharpness of the transition from the 1-halo to the outer profile, and on γ, describing the steepness of the profile at $r \sim r_{200m}$. We expressed γ as $\gamma = \gamma_0\nu_{vir}$, following DK14. Furthermore, as discussed in Sect. 4.6, we assumed Gaussian priors on F_t, β, and γ_0.

Equation (10) models the matter density distribution at $r > r_{200m}$, and it is expressed as a power-law multiplying the mean background density of the Universe, ρ_m. Following the DK14 prescription, we defined the pivot radius as 5 times r_{200m}. The parameters b_e and s_e characterise the amplitude and slope of the outer profile, respectively, and are treated as free parameters in our analysis. In simulations, both the bias parameter, b_e, and the slope, s_e, exhibit a mild dependence on the peak height (Diemer & Kravtsov 2014). While s_e shows only a weak redshift evolution, this dependence is somewhat stronger for b_e. Thus, in our modelling, we allowed b_e to vary as a function of redshift, assuming the following expression:

$$b_e = b_{e,0}\left[\frac{1+z}{1+z_{piv}}\right]^{b_{e,z}} .$$
(11)

where $z_{piv} = 0.4$. We note that, differently from the DK14 functional form, Eq. (10) does not include ρ_m as an additive term. In fact, the mass profile probes considered in this study, namely weak lensing and correlation function, measure the excess of mass compared to the background. On the other hand, as detailed in Sect. 4.5, the ρ_m contribution is considered in the

computation of the splashback radius. The six free parameters describing the halo profiles (F_t, β, γ_0, $b_{e,0}$, $b_{e,z}$, and s_e) are summarised in the top part of Table 2.

4.2. g_t model for individual haloes

The tangential reduced shear component of a halo, g_t, is expressed as (Seitz & Schneider 1997)

$$g_t(R, M, z) = \frac{\Delta\Sigma_t(R, M, z)\,\langle\Sigma_{\mathrm{crit}}^{-1}(z)\rangle}{1 - \Sigma(R, M, z)\,\langle\Sigma_{\mathrm{crit}}^{-1}(z)\rangle^{-1}\,\langle\Sigma_{\mathrm{crit}}^{-2}(z)\rangle}\,, \tag{12}$$

where R is the projected radius, Σ is the surface mass density, obtained by integrating Eq. (8) as

$$\Sigma(R, M, z) = 2\int_0^{R_{\max}} \mathrm{d}\chi\,\Delta\rho\left(\sqrt{R^2 + \chi^2}, M, z\right), \tag{13}$$

where we set $R_{\max} = 40\,h^{-1}\mathrm{Mpc}$ (following More et al. 2016; Baxter et al. 2017; Shin et al. 2019). In Eq. (12), $\Delta\Sigma_t$ is the excess surface mass density, having the expression

$$\Delta\Sigma_t(R) = \frac{2}{R^2}\int_0^R \mathrm{d}r\,r\,\Sigma(r) - \Sigma(R)\,. \tag{14}$$

In Eq. (12), $\langle\Sigma_{\mathrm{crit}}^{-\eta}\rangle$ is defined as

$$\langle\Sigma_{\mathrm{crit}}^{-\eta}(z)\rangle = \int_{z_g > z} \mathrm{d}z_g\,\Sigma_{\mathrm{crit}}^{-\eta}(z_g, z)\,n(z_g\,|\,z)\,, \tag{15}$$

where $\eta = 1, 2$, Σ_{crit} is given by Eq. (2), z_g is the galaxy redshift, while $n(z_g\,|\,z)$ is the normalised true background redshift distribution given a cluster redshift z, reconstructed through SOM (Sect. 2). We remark that Eq. (12) describes the reduced shear profiles of perfectly centred cluster detections. The total reduced shear includes the contribution by miscentred clusters and is expressed as follows:

$$g_{t,\mathrm{tot}} = (1 - f_{\mathrm{off}})\,g_t + f_{\mathrm{off}}\,g_{t,\mathrm{off}}\,, \tag{16}$$

where f_{off} is the fraction of miscentred clusters, g_t is given by Eq. (12), while $g_{t,\mathrm{off}}$ is the miscentred tangential reduced shear, whose derivation is detailed in Appendix A.

4.3. w_{cg} model for individual haloes

We express the 2D cluster-galaxy correlation function as follows (see Appendix B for its derivation):

$$w_{cg}(R, M, z) = \frac{\langle b_g(M, z)\rangle}{\rho_m(z)}\int_0^\infty \mathrm{d}z_g\,\Delta\rho\left[f(R, z_g, z), M, z\right] n(z_g)\,, \tag{17}$$

where $\Delta\rho$ is the DK14 profile (Eq. 8), while $n(z_g)$ is the normalised galaxy redshift distribution, reconstructed through SOM and shown in the middle panel of Fig. 1 (see also Sect. 2). For the integration in Eq. (17), we interpolated the discretised integrand. In Eq. (17), $f(R, z_g, z)$ is the physical distance between a

galaxy at z_g and a cluster at z, given a projected cluster-centric distance R, expressed as follows:

$$f(R, z_g, z) = \sqrt{R^2 + \left[\frac{\chi(z_g) - \chi(z)}{1 + z}\right]^2}\,, \tag{18}$$

where χ is the comoving distance. Furthermore, b_g in Eq. (17) is the galaxy bias, treated as independent of R (see Appendix B). As discussed in Sects. 4.4 and 4.6, we did not model the b_g dependence on the true halo mass and redshift. Instead, for each stack of clusters defined in bins of observed intrinsic richness λ_{ob}^* and cluster redshift z_{ob}, we introduced the average bias $\langle b_g(\Delta\lambda_{\mathrm{ob}}^*, \Delta z_{\mathrm{ob}})\rangle$ as a free parameter. We did not model miscentring in Eq. (17) because it primarily affects mass estimates. Since we adopted the mass posteriors from the g_t analysis as priors for the w_{cg} modelling (see Sect. 4.6), this effect is inherently accounted for in our approach.

4.4. Expected values for stacks of clusters

The expected value of the stacked reduced shear in a bin of observed intrinsic richness, $\Delta\lambda_{\mathrm{ob}}^*$, and redshift, Δz_{ob}, is expressed as

$$\langle g_t(R^{\mathrm{test}}, \Delta\lambda_{\mathrm{ob}}^*, \Delta z_{\mathrm{ob}})\rangle = \frac{\mathcal{P}_{\mathrm{cl}}(\Delta\lambda_{\mathrm{ob}}^*, \Delta z_{\mathrm{ob}})\,\langle\mathcal{P}_{\mathrm{bkg}}(\Delta z_{\mathrm{ob}})\rangle}{\langle n(\Delta\lambda_{\mathrm{ob}}^*, \Delta z_{\mathrm{ob}})\rangle} \times$$
$$\times \int_0^\infty \mathrm{d}z_{\mathrm{tr}}\,\frac{\mathrm{d}^2 V}{\mathrm{d}z_{\mathrm{tr}}\mathrm{d}\Omega}\int_0^\infty \mathrm{d}M\,g_{t,\mathrm{tot}}(R^{\mathrm{test}}, M, z_{\mathrm{tr}})\,\mathcal{S}(M, z_{\mathrm{tr}}, \Delta\lambda_{\mathrm{ob}}^*, \Delta z_{\mathrm{ob}})\,, \tag{19}$$

where $\mathcal{P}_{\mathrm{cl}}$ is the cluster sample purity, based on the Selection Function extrActor (SinFoniA, Maturi et al. 2019, 2025) mock catalogues, while $\mathcal{P}_{\mathrm{bkg}}$ is the purity of the background galaxy sample, derived through SOM. For details on these purity parameters, we refer to L25. In Eq. (19), z_{tr} is the true redshift, V is the co-moving volume, $\mathrm{d}\Omega$ is the solid angle element, M is the true mass, while $g_{t,\mathrm{tot}}$ is given by Eq. (16) and, in order to model geometric distortions, it is computed at the test radius R^{test},

$$R^{\mathrm{test}} = \theta D_l^{\mathrm{test}} = R^{\mathrm{fid}}\,\frac{D_l^{\mathrm{test}}}{D_l^{\mathrm{fid}}}\,. \tag{20}$$

Here, θ is the angular separation from the cluster centre, R^{fid} is the projected radius in the fiducial cosmology adopted for measurements (Sect. 3), while D_l^{fid} and D_l^{test} are the angular diameter distances in the fiducial and test cosmologies, respectively. The last factor in the integrand of Eq. (19) has the following expression:

$$\mathcal{S}(M, z_{\mathrm{tr}}, \Delta\lambda_{\mathrm{ob}}^*, \Delta z_{\mathrm{ob}}) = \frac{\mathrm{d}n(M, z_{\mathrm{tr}})}{\mathrm{d}M}\,\mathcal{B}_{\mathrm{HMF}}(M)\int_{\Delta z_{\mathrm{ob}}} \mathrm{d}z_{\mathrm{ob}}\,P(z_{\mathrm{ob}}|z_{\mathrm{tr}}) \times$$
$$\times \int_0^\infty \mathrm{d}\lambda_{\mathrm{tr}}^*\,C_{\mathrm{cl}}(\lambda_{\mathrm{tr}}^*, z_{\mathrm{tr}})\,P(\lambda_{\mathrm{tr}}^*|M, z_{\mathrm{tr}})\int_{\Delta\lambda_{\mathrm{ob}}^*} \mathrm{d}\lambda_{\mathrm{ob}}^*\,P(\lambda_{\mathrm{ob}}^*|\lambda_{\mathrm{tr}}^*, z_{\mathrm{tr}})\,, \tag{21}$$

where $\mathrm{d}n(M, z_{\mathrm{tr}})/\mathrm{d}M$ is the halo mass function, for which we adopt the model by Tinker et al. (2008), while $\mathcal{B}_{\mathrm{HMF}}(M)$ is the halo mass function bias. Following Costanzi et al. (2019), $\mathcal{B}_{\mathrm{HMF}}(M)$ is expressed as

$$\mathcal{B}_{\mathrm{HMF}}(M) = s\log\frac{M}{M^*} + q\,, \tag{22}$$

Table 2. Free base parameters considered in the analysis. Derived parameters, such as r_{sp}, are not reported.

Parameter	Description	g_t prior	w_{cg} prior	g_t posterior	w_{cg} posterior
F_t	Truncation factor of the 1-halo profile	$\mathcal{N}(1.495, 0.3)$	$\mathcal{N}(1.495, 0.3)$	$1.40^{+0.29}_{-0.22}$	$1.51^{+0.25}_{-0.21}$
β	Sharpness of the transition from 1-halo to two-halo	$\mathcal{N}(4, 1.6)$	$\mathcal{N}(4, 1.6)$	—	$3.35^{+0.94}_{-1.01}$
γ_0	Steepness of the profile at $r \sim r_{200m}$	$\mathcal{N}(4, 1.6)$	$\mathcal{N}(4, 1.6)$	—	—
$b_{e,0}$	Normalisation of the outer profile's amplitude	$[0.5, 4]$	$[0.5, 4]$	—	$1.97^{+0.23}_{-0.19}$
$b_{e,z}$	Redshift evolution of the outer profile's amplitude	$[-1, 1]$	$[-1, 1]$	—	—
s_e	Slope of the outer profile	$[0.5, 2]$	$[0.5, 2]$	—	$1.461^{+0.052}_{-0.046}$
f_{off}	Fraction of miscentred clusters	$\mathcal{N}(0.3, 0.1)$	—	—	—
σ_{off}	Miscentring scale (in $h^{-1}\mathrm{Mpc}$)	$[0, 0.5]$	—	$0.21^{+0.11}_{-0.11}$	—
A	Amplitude of the $\log \lambda^* - \log M_{200m}$ relation	$[-2, 2]$	g_t posterior	$-0.27^{+0.03}_{-0.05}$	—
B	Slope of the $\log \lambda^* - \log M_{200m}$ relation	$[0, 3]$	g_t posterior	$0.59^{+0.06}_{-0.05}$	—
C	Redshift evolution of the $\log \lambda^* - \log M_{200m}$ relation	$[-3, 3]$	g_t posterior	$0.28^{+0.29}_{-0.30}$	—
σ_{intr}	Intrinsic scatter of the $\log \lambda^* - \log M_{200m}$ relation	$[0.01, 0.5]$	g_t posterior	$0.07^{+0.04}_{-0.03}$	—
$\log c_0$	Amplitude of the $\log c_{200m} - \log M_{200m}$ relation	$[0, 1.3]$	$[0, 1.3]$	$0.68^{+0.17}_{-0.19}$	$0.82^{+0.19}_{-0.29}$
(s, q)	Parameters of the mass function correction factor	$\mathcal{N}(\mu_{HMF}, C_{HMF})$	$\mathcal{N}(\mu_{HMF}, C_{HMF})$	—	—
$\log b_{g,0}$	Logarithmic amplitude of the galaxy bias function	—	$[-3, 1]$	—	$0.068^{+0.062}_{-0.067}$
b_{g,λ^*}	λ^* evolution of the galaxy bias function	—	$[-2, 2]$	—	$-0.10^{+0.11}_{-0.11}$
$b_{g,z}$	z evolution of the galaxy bias function	—	$[-2, 2]$	—	$0.31^{+0.35}_{-0.33}$

Notes. In the first and second columns we list the symbols and descriptions of the parameters, respectively. The third and fourth columns report the parameter priors adopted for the modelling of g_t and w_{cg}, respectively. Here, a range represents a uniform prior, while $\mathcal{N}(\mu, \sigma)$ stands for a Gaussian prior with mean μ and standard deviation σ. In the last two columns, we show the median values of the 1D marginalised posteriors, along with the 16th and 84th percentiles. The posterior is not reported in cases where it closely aligns with the prior.

where M^* is expressed in $h^{-1}\mathrm{M}_\odot$ and $\log M^* = 13.8$, q and s are free parameters of the model (see Sect. 4.6). In Eq. (21), z_{ob}, λ^*_{ob}, and λ^*_{tr} are the observed redshift, observed intrinsic richness, and true intrinsic richness, respectively. $P(z_{ob}|z_{tr})$ is a Gaussian probability density function with mean corresponding to z_{tr} and a standard deviation of $0.014(1 + z_{tr})$ (see Sect. 2), while $P(\lambda^*_{ob}|\lambda^*_{tr}, z_{tr})$ is a Gaussian whose mean is expressed as

$$\mu_{\lambda^*} = \lambda^*_{tr} + \lambda^*_{tr} \exp[-\lambda^*_{tr}(A_\mu + B_\mu z_{tr})], \tag{23}$$

while its standard deviation has the form

$$\sigma_{\lambda^*} = A_\sigma \lambda^*_{tr} \exp(-B_\sigma \lambda^*_{tr}). \tag{24}$$

In Eqs. (23) and (24), $A_\mu = 0.198$, $B_\mu = -0.179$, $A_\sigma = 0.320$, and $B_\sigma = 0.011$. We refer to L25 for details on the derivation of $P(\lambda^*_{ob}|\lambda^*_{tr}, z_{tr})$, its coefficients, and of the cluster sample completeness, C_{cl}, appearing in Eq. (21) and based on SinFoniA. The probability density distribution $P(\lambda^*_{tr}|M, z_{tr})$ follows a log-normal form, with its mean determined by the $\log \lambda^* - \log M_{200m}$ scaling relation and its dispersion set by the intrinsic scatter σ_{intr}:

$$P(\lambda^*_{tr}|M, z_{tr}) = \frac{1}{\ln(10)\lambda^*_{tr}\sqrt{2\pi}\sigma_{intr}} \exp\left(-\frac{[\log \lambda^*_{tr} - \mu(M, z_{tr})]^2}{2\sigma^2_{intr}}\right). \tag{25}$$

Here, $\mu(M, z_{tr})$ is the mean of the distribution, expressed as

$$\mu(M, z_{tr}) = A + B \log \frac{M}{M_{piv}} + C \log \frac{H(z_{tr})}{H(z_{piv})} + \log \lambda^*_{piv}, \tag{26}$$

where $M_{piv} = 10^{14} h^{-1} M_\odot$, $z_{piv} = 0.4$, and $\lambda^*_{piv} = 50$ are the redshift, mass, and intrinsic richness pivots, respectively. The penultimate term in Eq. (26), including the Hubble function $H(z)$,

captures deviations from the predictions from the self-similar growth scenario (Sereno & Ettori 2015a). As described in Sect. 4.6, A, B, C, and σ_{intr} in Eqs. (25) and (26) are treated as free parameters in our modelling (see also Table 2). Lastly, in Eq. (19), $\langle n(\Delta\lambda^*_{ob}, \Delta z_{ob}) \rangle$ is the expected density of observed haloes and has the form

$$\langle n(\Delta\lambda^*_{ob}, \Delta z_{ob}) \rangle = \int_0^\infty dz_{tr} \frac{d^2 V}{dz_{tr} d\Omega} \int_0^\infty dM\, \mathcal{S}(M, z_{tr}, \Delta\lambda^*_{ob}, \Delta z_{ob}). \tag{27}$$

The expected cluster-galaxy correlation function in the bins $\Delta\lambda^*_{ob}$ and Δz_{ob} is expressed as

$$\langle w_{cg}(R^{test}, \Delta\lambda^*_{ob}, \Delta z_{ob}) \rangle = -\mathcal{I}(\Delta\lambda^*_{ob}, \Delta z_{ob}) + \frac{\langle b_g(\Delta\lambda^*_{ob}, \Delta z_{ob}) \rangle}{\langle n(\Delta\lambda^*_{ob}, \Delta z_{ob}) \rangle} \times$$

$$\times \int_0^\infty dz_{tr} \frac{d^2 V}{dz_{tr} d\Omega} \int_0^\infty dM\, \hat{w}_{cg}(R^{test}, M, z_{tr}) \mathcal{S}(M, z_{tr}, \Delta\lambda^*_{ob}, \Delta z_{ob}), \tag{28}$$

where $\langle b_g \rangle$ is the average galaxy bias, which follows the relation

$$\langle b_g(\Delta\lambda^*_{ob}, \Delta z_{ob}) \rangle = b_{g,0} \left(\frac{\bar{\lambda}^*_{ob}}{\lambda^*_{piv}}\right)^{b_{g,\lambda^*}} \left(\frac{1 + \bar{z}_{ob}}{1 + z_{piv}}\right)^{b_{g,z}}. \tag{29}$$

Here, λ^*_{piv} and z_{piv} are the pivot values adopted also in Eq. (26), while $\bar{\lambda}^*_{ob}$ and $\bar{z}_{ob}$ are the median values within $\Delta\lambda^*_{ob}$ and Δz_{ob}, respectively, listed in Table 1. By modelling the cluster stacks

separately, we verified that Eq. (29) describes well the mass proxy and redshift dependence of b_g. In Eq. (28), $\hat{w}_{cg}$ is the cluster-galaxy correlation function in Eq. (17) where we impose $\langle b_g(M, z) \rangle = 1$, and $\mathcal{I}$ is the integral constraint, expressed as (Roche & Eales 1999; Adelberger et al. 2005; Coupon et al. 2012):

$$\mathcal{I}(\Delta\lambda^*_{ob}, \Delta z_{ob}) = \langle b_g(\Delta\lambda^*_{ob}, \Delta z_{ob}) \rangle \times$$
$$\times \frac{\sum_j \mathcal{R}_c \mathcal{R}_g(R_j|\Delta z_{ob}) \langle \tilde{w}_{cg}(R_j, \Delta\lambda^*_{ob}, \Delta z_{ob}) \rangle}{\sum_j \mathcal{R}_c \mathcal{R}_g(R_j|\Delta z_{ob})}, \tag{30}$$

where $\mathcal{R}_c \mathcal{R}_g$ is the normalised number of random cluster - random galaxy pairs, where random redshifts follow the observed distribution within the bin Δz_{ob}. Moreover, $\langle \tilde{w}_{cg} \rangle$ is obtained by imposing $\mathcal{I}(\Delta\lambda^*_{ob}, \Delta z_{ob}) = 0$ in Eq. (28), while j runs over the number of cluster-centric radial bins. Here, the minimum radial scale considered is $400\ h^{-1}$kpc, matching the one adopted for the measurements (Sect. 3). The radial upper limit considered in Eq. (30) is derived as

$$R_{lim}(z) = D_l(z)\,\theta_{lim}, \tag{31}$$

where D_l is the angular diameter distance, computed at the median cluster redshifts listed in Table 1, while θ_{lim} represents the angular extension of the smallest side of the KiDS angular mask. We remark that KiDS is divided into two stripes, with $\theta_{lim} = 8.5$ deg on average (Kuijken et al. 2019). We adopted this θ_{lim} value in Eq. (31), which yields $R_{lim} \simeq 70\ h^{-1}$Mpc for $z_{ob} \in [0.1, 0.3)$, $R_{lim} \simeq 110\ h^{-1}$Mpc for $z_{ob} \in [0.3, 0.45)$, and $R_{lim} \simeq 150\ h^{-1}$Mpc for $z_{ob} \in [0.45, 0.8]$. Assuming the best-fit parameters of the w_{cg} modelling in Eq. (30), we find that $\mathcal{I}(\Delta\lambda^*_{ob}, \Delta z_{ob}) \simeq 10^{-2}$ in all cluster stacks. This is the same order of magnitude as the w_{cg} measurements at large radii and low-to-intermediate redshifts (see Fig. 2).

In the reduced shear and correlation function models appearing in Eqs. (19) and (28), we assumed the following log-linear model for the $c_{200m} - M_{200m}$ relation:

$$\log c_{200m} = \log c_0 + c_M \log \frac{M}{M_{piv}} + c_z \log \frac{1 + z_{tr}}{1 + z_{piv}}, \tag{32}$$

where M_{piv} and z_{piv} are the same as those assumed in Eq. (26). As discussed in Sect. 4.6, $\log c_0$ is a free parameter in the analysis, while c_M and c_z are fixed to the fiducial values by Duffy et al. (2008).

4.5. Splashback radius estimator

The main goal of this study consists in constraining the following relation (introduced by More et al. 2015):

$$\langle \mathcal{R}_{sp}(\Delta\lambda^*_{ob}, \Delta z_{ob}) \rangle = A_{sp} \left[1 + B_{sp} \exp \left(-\frac{\langle \nu_{200m}(\Delta\lambda^*_{ob}, \Delta z_{ob}) \rangle}{2.44} \right) \right], \tag{33}$$

where A_{sp} and B_{sp} are free parameters, while $\langle \mathcal{R}_{sp} \rangle$ and $\langle \nu_{200m} \rangle$ are the average normalised splashback radius and the average peak height, respectively. In our analysis, we derive $\langle \mathcal{R}_{sp} \rangle$ and $\langle \nu_{200m} \rangle$ posteriors and constrain A_{sp} and B_{sp}. Specifically, $\langle \mathcal{R}_{sp} \rangle$

is expressed as

$$\langle \mathcal{R}_{sp}(\Delta\lambda^*_{ob}, \Delta z_{ob}) \rangle \equiv \left\langle \frac{r_{sp}}{r_{200m}}(\Delta\lambda^*_{ob}, \Delta z_{ob}) \right\rangle =$$
$$= \frac{\int_0^\infty dz_{tr} \frac{d^2V}{dz_{tr}d\Omega} \int_0^\infty dM\,\mathcal{R}_{sp}(M, z_{tr})\,\mathcal{S}(M, z_{tr}, \Delta\lambda^*_{ob}, \Delta z_{ob})}{\langle n(\Delta\lambda^*_{ob}, \Delta z_{ob}) \rangle}, \tag{34}$$

where

$$\mathcal{R}_{sp}(M, z_{tr}) = \frac{r_{sp}(M, z_{tr})}{r_{200m}(M, z_{tr})}. \tag{35}$$

Here, we define the splashback radius of a halo as

$$r_{sp}(M, z_{tr}) \equiv \min \left[\frac{d \log \left[\Delta\rho(r, M, z_{tr}) + \rho_m(z_{tr}) \right]}{d \log r} \right], \tag{36}$$

where $\Delta\rho(r, M, z_{tr})$ is given by Eq. (8). Equation (36) does not include the contribution by halo miscentring, as it affects scales much smaller than r_{sp} and can be therefore neglected. We evaluate Eq. (34) at each step of the Markov chain Monte Carlo (MCMC). By replacing $\mathcal{R}_{sp}(M, z_{tr})$ in Eq. (34) with $\nu_{200m}(M, z_{tr})$, $r_{sp}(M, z_{tr})$, or M_{200m}, we derived the expected value of ν_{200m} (appearing in Eq. 33), r_{sp}, or M_{200m}, respectively, in bins of λ^*_{ob} and z_{ob}.

We emphasise that Eq. (34) removes any dependence on the radial binning scheme. While stacking clusters as a function of r/r_{200m} could in principle enhance the signal-to-noise of r_{sp} (Diemer & Kravtsov 2014), this approach is compromised for observational data due to noisy r_{200m} estimates. Equation (34) solves this issue, as it models the average profile of a reconstructed population of dark matter haloes. Conversely, in simulations, average profiles of cluster ensembles are modelled as a single profile, thanks to the reduced scatter on r_{200m}.

4.6. Likelihood and priors

In this work, we analysed g_t and w_{cg} separately to compare two independent estimates of r_{sp}. For both these probes, we performed a joint Bayesian analysis of all the cluster stacks, by means of an MCMC algorithm. The likelihood function of a probe is expressed as

$$\mathcal{L} = \prod_{i=1}^{N_{\lambda^*}} \prod_{j=1}^{N_z} \mathcal{L}_{ij}, \tag{37}$$

where N_{λ^*} and N_z are the numbers of cluster intrinsic richness and redshift bins used for the stacked measurements, respectively, while $\mathcal{L}_{ij}$ is a Gaussian likelihood function defined as

$$\mathcal{L}_{ij} \propto \exp(-\chi^2_{ij}/2), \tag{38}$$

with

$$\chi^2_{ij} = \sum_{k=1}^{N_R} \sum_{l=1}^{N_R} \left(O_{ijk} - \mathcal{M}_{ijk} \right) C^{-1}_{ijkl} \left(O_{ijl} - \mathcal{M}_{ijl} \right). \tag{39}$$

Here, O_{ijk} is either the stacked weak-lensing (Eq. 5) or the cluster-galaxy correlation (Eq. 7) measurement, while $\mathcal{M}_{ijk}$ is the corresponding model, namely Eq. (19) or Eq. (28), respectively. The indices k and l run over the number of radial bins, N_R, and C^{-1}_{ijkl} is the inverse of the covariance matrix. Following
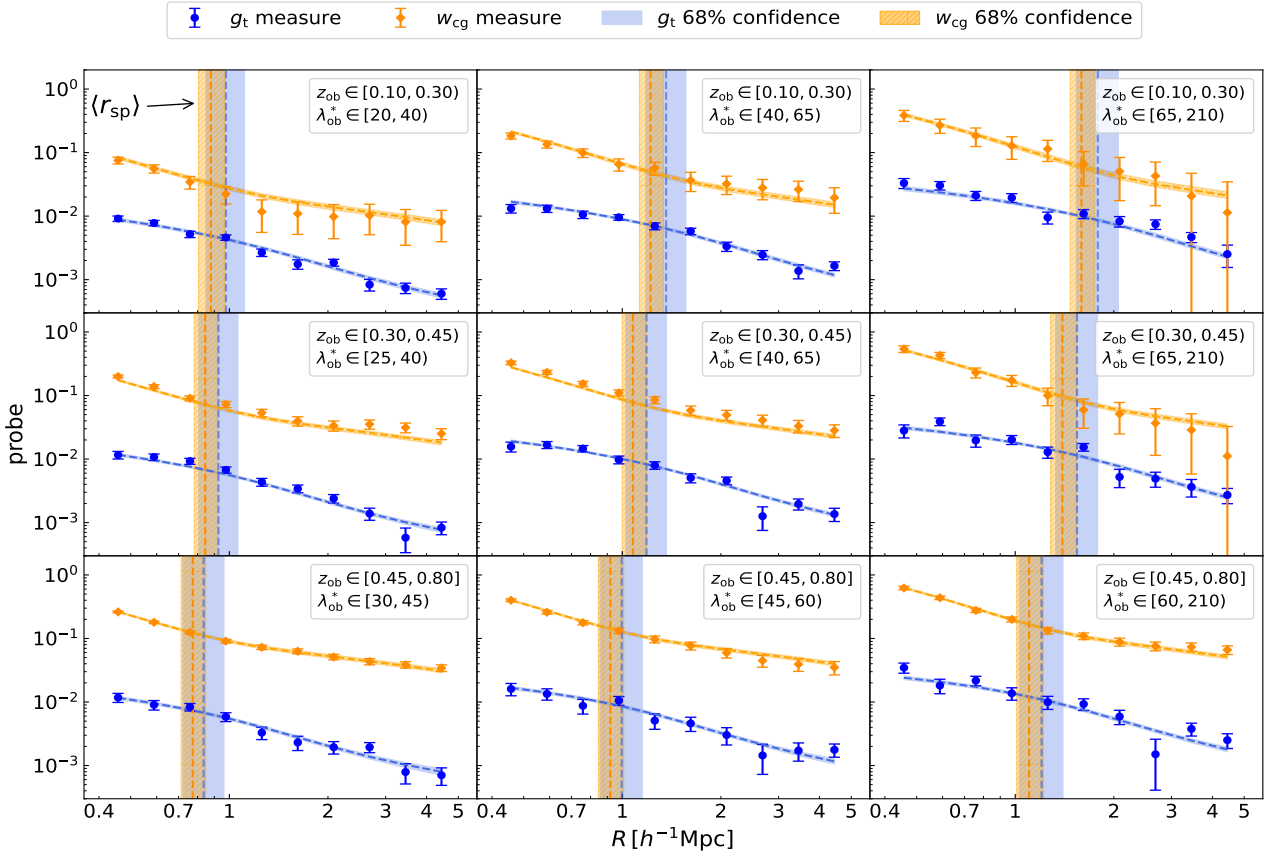
Fig. 2. Measurements of g_t (blue dots) and w_{cg} (orange diamonds) profiles of the AMICO KiDS-1000 galaxy clusters, in bins of z (increasing from top to bottom) and λ^* (increasing from left to right). The error bars are the sum of statistical errors and residual uncertainties coming from systematic errors (see Sect. 4.6). The bands superimposed to the measurements represent the 68% confidence levels of the g_t (blue) and w_{cg} (orange) models. The vertical bands show the 68% confidence of the splashback radius, derived from the modelling of g_t (blue) and w_{cg} (orange). The dashed lines represent median values.

Hartlap et al. (2007), we applied the standard correction when inverting the covariance matrix. In particular, C_{ijkl} is defined as

$$C_{ijkl} = C_{ijkl}^{\text{stat}} + C_{ijkl}^{\text{sys}}, \tag{40}$$

where C_{ijkl}^{stat} is the statical part of the covariance, estimated through resampling as discussed in Sect. 3, while C_{ijkl}^{sys} accounts for residual uncertainties on systematic errors that are not included in the model. In the case of g_t, this covariance contribution is written as

$$C_{ijkl}^{\text{sys},g_t} = (\sigma_m^2 + \sigma_{\text{SOM}}^2 + \sigma_{\text{OP}}^2)\, g_{t,k}^{\text{ob}}(\Delta\lambda_{\text{ob},i}^*, \Delta z_{\text{ob},j})\, g_{t,l}^{\text{ob}}(\Delta\lambda_{\text{ob},i}^*, \Delta z_{\text{ob},j}), \tag{41}$$

where g_t^{ob} is the observed stacked reduced shear, $\sigma_m = 0.02$ is the uncertainty on the multiplicative shear bias, corresponding to the largest multiplicative bias uncertainty reported across the tomographic bins analysed by Giblin et al. (2021). Furthermore, σ_{SOM} accounts for the uncertainty on the SOM-reconstructed background redshift distributions, amounting to $\sigma_{\text{SOM}} = 0.01$ for the first two cluster redshift bins and to $\sigma_{\text{SOM}} = 0.04$ for the last one (see Sect. 4.4 in L25), while $\sigma_{\text{OP}} = 0.03$ is the residual uncertainty due to orientation and projection effects (see Sect. 5.4 in L25).

Measurements of w_{cg} are not affected by multiplicative shear biases. We also ignored orientation and projection effects in this case, assuming that their impact is absorbed by the free galaxy

bias in Eq. (28). The impact of this approach on galaxy bias constraints shall be tested in future studies. Conversely, we included the contribution to w_{cg} measurements due to the uncertainty on the mean of the SOM-reconstructed $n(z_g)$, amounting to 2% (Hildebrandt et al. 2021). To this end, we estimated $\langle w_{cg}(R, \Delta\lambda_{\text{ob}}^*, \Delta z_{\text{ob}})\rangle$ in Eq. (28) at the model best-fit parameters, using the reconstructed $n(z_g)$ from Sect. 2 in Eq. (17). We then repeated this process while shifting $n_{\text{bkg}}(z_g)$ by ±2% of its mean. This yielded a relative uncertainty on w_{cg} which is approximately constant with R and λ_{ob}^*, amounting to 3% for the first two cluster redshift bins and 2% for the last one. Thus, the residual systematics term in the case of w_{cg} has the following expression:

$$C_{ijkl}^{\text{sys},w_{cg}} = \sigma_{\text{SOM}}^2\, \omega_{cg,k}^{\text{ob}}(\Delta\lambda_{\text{ob},i}^*, \Delta z_{\text{ob},j})\, \omega_{cg,l}^{\text{ob}}(\Delta\lambda_{\text{ob},i}^*, \Delta z_{\text{ob},j}), \tag{42}$$

where w_{cg}^{ob} is the observed cluster-galaxy correlation function, $\sigma_{\text{SOM}} = 0.03$ for $z_{\text{ob}} \in [0.1, 0.3]$ and $z_{\text{ob}} \in [0.3, 0.45]$, while $\sigma_{\text{SOM}} = 0.02$ for $z_{\text{ob}} \in [0.45, 0.8]$.

The parameter priors adopted in the analysis are reported in Table 2. We assumed a Gaussian prior on the truncation factor of the 1-halo term, F_t, in Eq. (8), with mean 1.495 (following DK14) and standard deviation 0.3 (corresponding to that assumed by L25, in the case of M_{200m}), imposing also $F_t > 0$. Gaussian priors were adopted also on the parameters of the transition factor (Eq. 9), namely γ_0, appearing in the relation $\gamma = \gamma_0 \nu_{\text{vir}}$ (see Sect. 4.1), and β, both having mean 4 (following DK14) and standard deviation 1.6 (following More et al. 2016; Shin et al. 2019; Murata et al. 2020; Rana et al. 2023). For the

outer profile parameters (Eq. 10), as introduced in Sect. 4.1, we assumed that s_e is independent of mass and redshift, and adopted a flat prior on this parameter. On the other hand, b_e varies with redshift (Eq. 11), and flat priors are adopted for its amplitude, $b_{e,0}$, and redshift scaling, $b_{e,z}$.

The fraction of miscentred clusters, f_{off}, in Eq. (16) is assigned a Gaussian prior with mean 0.3 and standard deviation 0.1, imposing also $f_{off} > 0$, while the miscentring scale, σ_{off}, in Eq. (A.1) is given the uniform prior $[0, 0.5]$ h^{-1}Mpc. These priors are motivated by previous studies of centre offsets in simulations (Yan et al. 2020; Sommer et al. 2024) and observations across various mass density tracers (Saro et al. 2015; Zhang et al. 2019; Seppi et al. 2023; Ding et al. 2025). In the g_t modelling, we assumed flat priors on the $\log \lambda^* - \log M_{200m}$ scaling relation parameters (Eqs. 25 and 26), namely A, B, C, and σ_{intr}. On the other hand, to analyse w_{cg} we assumed the g_t posteriors on these parameters as priors. A flat prior is used for the amplitude of the $\log c_{200m} - \log M_{200m}$ relation (Eq. 32). In the latter relation, we fixed $c_M = -0.107$ and $c_z = -1.16$ (following Duffy et al. 2008). We expect that our priors on σ_{intr} and c_{200m} account for theoretical uncertainties in baryonic effects on cluster profiles (Schaller et al. 2015; Henson et al. 2017; Lee et al. 2018; Beltz-Mohrmann & Berlind 2021; Shao & Anbajagane 2024).

In the w_{cg} modelling, we assumed flat priors on $b_{g,0}$, b_{g,λ^*}, and $b_{g,z}$, which enter the relation between the average galaxy bias, $\langle b_g(\Delta \lambda^*_{ob}, \Delta z_{ob})\rangle$, and cluster observables (Eq. 29). The $\mathcal{B}_{HMF}$ factor in Eq. (22) provides a correction to the standard Tinker et al. (2008) halo mass function. For the parameters s and q, we employed the Costanzi et al. (2019) prescription, assigning a bivariate Gaussian prior with mean values $(0.037, 1.008)$ and covariance matrix C_{HMF} expressed as

$$C_{HMF} = \begin{pmatrix} 0.00019 & 0.00024 \\ 0.00024 & 0.00038 \end{pmatrix}. \tag{43}$$

Although baryonic physics uncertainties are not taken into account in this prescription, they are negligible compared to the precision of the $\mathcal{B}_{HMF}$ measurement (see Costanzi et al. 2019, and references therein).

5. Results

In the modelling presented here, we adopted a flat ΛCDM cosmological model assuming the median values of the posteriors derived by L25, namely $\Omega_m = 0.22$ and $\sigma_8 = 0.86$. The other cosmological parameters were fixed to the results by Planck Collaboration et al. (2020, Table 2, TT, TE + EE + lowE + lensing, referred to as Planck18 hereafter). Figure 2 shows the g_t and w_{cg} measurements against the corresponding best-fit models. The $\langle r_{sp}\rangle$ estimates are shown as vertical bands, and are derived by computing the model described in Sect. 4.5 at each MCMC step. The results presented in this section on splashback radii, masses, and other derived quantities are reported also in Table 1. The robustness of the results against our modelling choices is discussed in Appendix C.

The top-left panel of Fig. 3 displays our constraints on $\langle \mathcal{R}_{sp}\rangle \equiv \langle r_{sp}/r_{200m}\rangle$, based on the methods outlined in Sect. 4.5. Specifically, we first obtained the posteriors on $\langle \mathcal{R}_{sp}\rangle$ and $\langle \nu_{200m}\rangle$ in each stack using Eq. (34), and then constrained A_{sp} and B_{sp} in Eq. (33) through an MCMC algorithm. In this process, we ignored the statistical uncertainty on $\langle \nu_{200m}\rangle$, corresponding to about 2%. We obtained the following constraints:

$$A_{sp}^{g_t} = 0.91^{+0.30}_{-0.30}, \quad B_{sp}^{g_t} = 0.49^{+1.63}_{-0.84}$$
$$A_{sp}^{w_{cg}} = 0.87^{+0.20}_{-0.21}, \quad B_{sp}^{w_{cg}} = 0.30^{+0.97}_{-0.59}, \tag{44}$$

where the g_t and w_{cg} superscripts represent the results derived from the modelling of weak-lensing and cluster-galaxy correlation function measurements, respectively. As we can see in the top-left panel of Fig. 3, our estimates of $\mathcal{R}_{sp}$ derived from these two probes are consistent within 1σ. This agreement between the two probes is in line with the findings of previous studies (Chang et al. 2018; Shin et al. 2021). Furthermore, as reported in Table 1, we find no significant trends of $\mathcal{R}_{sp}$ with redshift or intrinsic richness, indicating that r_{sp} and r_{200m} share similar dependencies on M_{200m} and z, in agreement with simulation predictions (More et al. 2015; Diemer 2020a).

Compared to the $\mathcal{R}_{sp}$ constraints from Giocoli et al. (2024) shown in Fig. 3, based on weak-lensing measurements in KiDS-DR3, our g_t modelling yields results that agree within 1σ for $\nu_{200m} > 3$, reducing to 2σ agreement at lower ν_{200m}. We verified the consistency within 1σ between our r_{sp} values and those from Giocoli et al. (2024). Furthermore, our mass constraints agree with those by L25 (see Appendix C). Thus, we conclude that the observed small shift in $\mathcal{R}_{sp}$ aligns with the cluster mass discrepancy between KiDS-1000 and KiDS-DR3 reported by L25. In that work, the KiDS-1000 analysis yields lower masses at the low-mass end. These lower masses imply smaller r_{200m} values, which in turn explain the larger $\mathcal{R}_{sp}$ we find compared to Giocoli et al. (2024). L25 ascribe these mass differences to improved systematic uncertainty modelling in KiDS-1000 (see Appendix C in that reference). The modelling of w_{cg} provides $\mathcal{R}_{sp}$ constraints in better agreement with Giocoli et al. (2024). As discussed below, this agreement originates mainly from the lower r_{sp} values derived from cluster-galaxy correlation function measurements, which we attribute to dynamical friction. Indeed, g_t probes the total matter distribution and is insensitive to galaxy-specific dynamical processes, while w_{cg} traces the spatial distribution of satellite galaxies. Dynamical friction acts on these satellites, causing them to lose kinetic energy and sink inward. This shifts the splashback radius traced by w_{cg} to smaller values.

The precision of the $\mathcal{R}_{sp} - \nu_{200m}$ relation parameters, reported in Eq. (44), aligns with the findings of Giocoli et al. (2024). Our analysis, however, incorporates a more comprehensive marginalisation over statistical uncertainties, including those from the transition factor parameters (Eq. 9), the halo miscentring (Sect. 4.2), the intrinsic scatter of the $\log \lambda^* - \log M_{200m}$ relation (Eq. 25), and the halo mass function correction (Eqs. 22 and 43). We also applied more conservative λ^* cuts.

The $\mathcal{R}_{sp}$ models in the top-left panel of Fig. 3 are computed across the mass range of our sample, $M_{200m} \in [0.4, 20]$ $10^{14} h^{-1} M_{\odot}$, which is derived from individual cluster mass estimates based on Eq. (54) in L25 and on the parameter posteriors obtained from the g_t modelling (Table 2). The theoretical models shown in the figure, by More et al. (2015) and Diemer (2020a), are computed at $z = 0.45$, which corresponds to the midpoint of the redshift range covered by our cluster sample. We remark that the redshift dependence of these models is very mild. Our constraints are in good agreement with these theoretical predictions. The largest deviations appear for the w_{cg} results at $\nu_{200m} < 3$, reaching 2σ with Diemer (2020a) at $\nu_{200m} \sim 2$.

The top-left panel of Fig. 3 also shows the comparison with literature results based on X-ray (Umetsu & Diemer 2017; Contigiani et al. 2019; Bianconi et al. 2021; Rana et al. 2023; Joshi et al. 2025), Sunyaev-Zeldovich (SZ, Zürcher & More 2019; Shin et al. 2019, 2021), and optical (More et al. 2016; Baxter et al. 2017; Chang et al. 2018; Murata et al. 2020) samples of
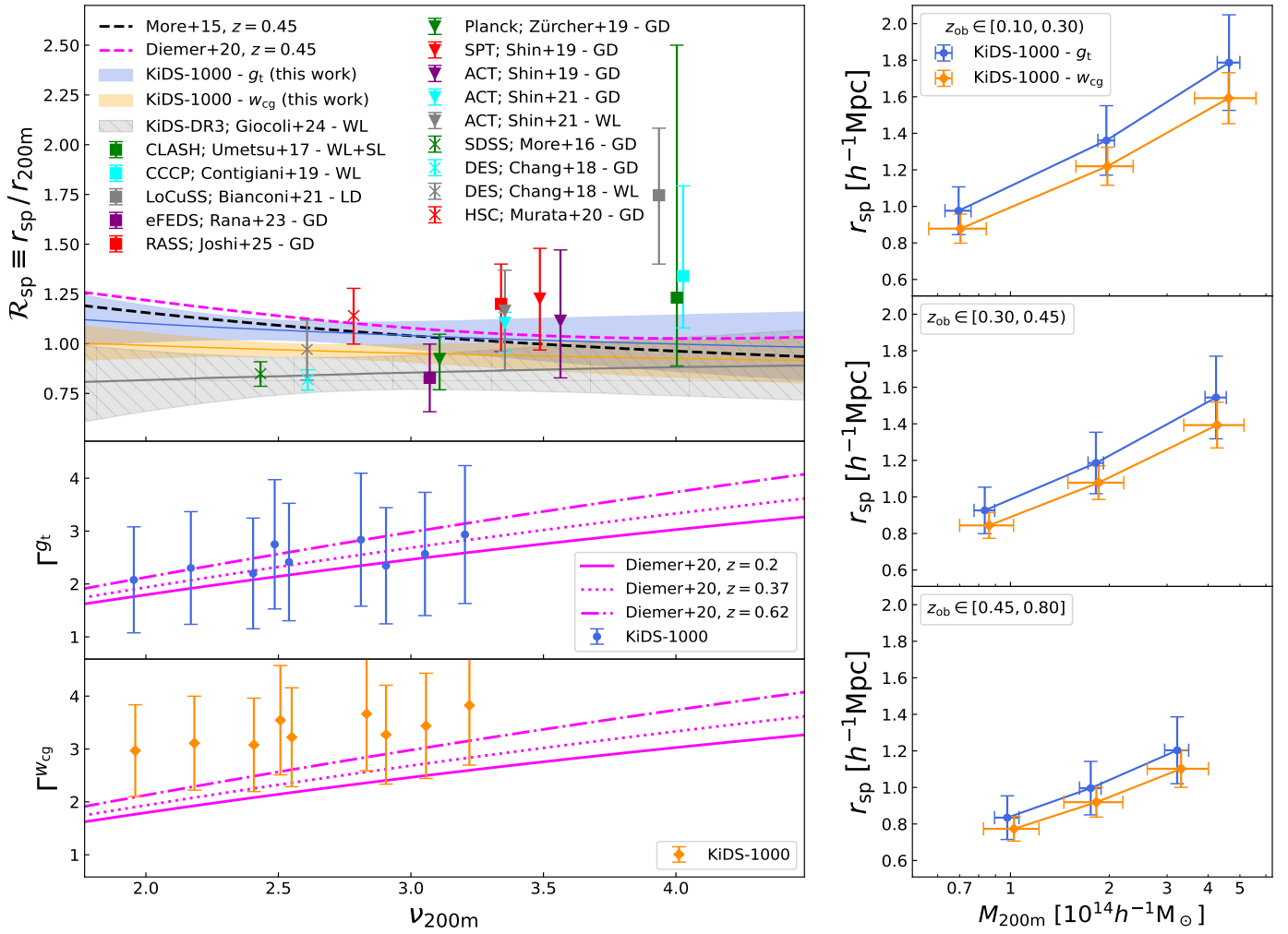
Fig. 3. Left panels: Constraints on the ratio of r_{sp} to r_{200m} as a function of ν_{200m} (top panel), obtained from the modelling of g_t (blue band) and w_{cg} (orange band) presented in this work, and by Giocoli et al. (2024) in KiDS-DR3 (grey band). The median theoretical models by More et al. (2015) (black dashed line) and Diemer (2020a) (magenta dashed line) are shown. Both models are computed at $z = 0.45$. Squares represent the results from X-ray-selected clusters by Umetsu & Diemer (2017, green), Contigiani et al. (2019, cyan), Bianconi et al. (2021, grey), Rana et al. (2023, purple), Joshi et al. (2025, red). Triangles display results from SZ-selected cluster catalogues by Zürcher & More (2019, green), Shin et al. (2019, red and purple), Shin et al. (2021, cyan and grey). Crosses show the results from optically-selected clusters by More et al. (2016); Baxter et al. (2017, green), Chang et al. (2018, cyan and grey), Murata et al. (2020, red). The probes used in these analyses, namely weak lensing (WL), strong lensing (SL), luminosity distribution (LD), and galaxy distribution (GD), are reported in the legend. Mass accretion rates from g_t and w_{cg} measurements are shown in the middle and bottom panels, respectively. Here, the model by Diemer (2020a) is shown, computed at $z = 0.2$ (solid lines), $z = 0.37$ (dotted lines), and $z = 0.62$ (dash-dotted lines). Right panels: r_{sp} derived from the modelling of g_t (blue dots) and w_{cg} (orange diamonds), as a function of M_{200m} and for $z_{ob} \in [0.1, 0.3)$ (top panel), $z_{ob} \in [0.3, 0.45)$ (middle panel), $z_{ob} \in [0.45, 0.8]$ (bottom panel).

galaxy clusters.[3] We find general agreement with these literature results. The largest discrepancies arise against the results by More et al. (2016) and Chang et al. (2018), based on cluster member galaxy distributions. This may be explained in part by dynamical friction, which has a greater effect on the galaxy sam-

ples used in those studies. In fact, More et al. (2016) and Chang et al. (2018) used shallower galaxy samples, with a magnitude limit of $i < 21.5$. Compared to our work, this implies a selection of more massive galaxies, for which the impact of dynamical friction is stronger. Future photometric surveys will allow for a detailed investigation of the effects by dynamical friction.

As displayed in the top and middle panels of Fig. 4, the precision on $\mathcal{R}_{sp}$ and r_{sp} derived from the modelling of g_t and w_{cg} is constant with z and M_{200m}. It amounts to 14% for g_t and to 10% for w_{cg}. These precisions are among the best available in the literature to date. Furthermore, these results show that w_{cg} is a stronger probe of the splashback radius, as it directly constrains the infalling term parameters, which are not accessible via weak-lensing observations (see Appendix D).

The right panels of Fig. 3 show that r_{sp} estimates from w_{cg} are systematically lower than those from the g_t modelling, al-

---

[3] The legend in the top-left panel of Fig. 3 reports the surveys these works are based on, namely the Cluster Lensing And Supernova survey with Hubble (CLASH, Postman et al. 2012), the Canadian Cluster Comparison Project (CCCP, Hoekstra et al. 2012), the Local Cluster Substructure Survey (LoCuSS, Böhringer et al. 2004), the eROSITA final equatorial depth survey (eFEDS, Bulbul et al. 2022), the ROSAT All-Sky Survey (RASS, Voges et al. 1999), Planck (Planck Collaboration et al. 2020), the South Pole Telescope (SPT, Bleem et al. 2015) survey, the Atacama Cosmology Telescope (ACT, Hilton et al. 2018) survey, the Sloan Digital Sky Survey (SDSS, Aihara et al. 2011), the Dark Energy Survey (DES, The Dark Energy Survey Collaboration 2005), and the Hyper Suprime-Cam (HSC, Miyazaki et al. 2012) survey.
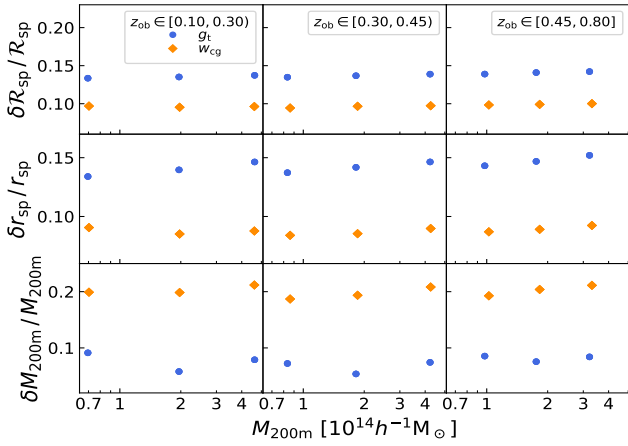
Fig. 4. Precision of the $\mathcal{R}_{sp}$ (top panels), r_{sp} (middle panels), and M_{200m} (bottom panels) constraints, obtained from the modelling of g_t (blue dots) and w_{cg} (orange diamonds), for $z_{ob} \in [0.1, 0.3)$ (left panels), $z_{ob} \in [0.3, 0.45)$ (central panels), and $z_{ob} \in [0.45, 0.8]$ (right panels).

though the values remain consistent within 1σ. This small offset can be attributed to dynamical friction affecting cluster members (Diemer et al. 2017; Chang et al. 2018), which also causes haloes to appear more concentrated. Figure 3 displays also an agreement on the M_{200m} constraints derived from the two probes. As we detail in Appendix D, the larger M_{200m} uncertainties derived from w_{cg}, displayed in the bottom panels of Fig. 4, are attributed to the differences in the constraints on the A and σ_{intr} parameters, appearing in the $\log \lambda^* - \log M_{200m}$ relation. The right panels of Fig. 3 also show that r_{sp} mildly decreases with redshift, as higher redshifts correspond to larger halo mass accretion rates, leading to smaller splashback radii (Diemer & Kravtsov 2014; Diemer et al. 2017).

More et al. (2015) derived the following expression for the dimensionless mass accretion rate, Γ,

$$\Gamma \equiv \frac{\Delta \log M_{vir}}{\Delta \log a} = 0.935 - 3.04 \ln\left(\frac{\mathcal{R}_{sp}}{0.54 + 0.286\, \Omega_m(z)} - 1\right), \quad (45)$$

where a is the scale factor. We computed Γ posteriors by injecting $\langle \mathcal{R}_{sp}(\Delta \lambda^*_{ob}, \Delta z_{ob}) \rangle$ values, derived from Eq. (34) at each MCMC step, into Eq. (45). Furthermore, $\Omega_m(z)$ in Eq. (45) is computed at the median cluster redshifts reported in Table 1. As shown in the middle and bottom left panels of Fig. 3, our constraints on Γ^{g_t} and $\Gamma^{w_{cg}}$, derived from the modelling of g_t and w_{cg}, respectively, agree with the theoretical model by Diemer (2020a). This agreement is expected, as our $\mathcal{R}_{sp}$ results are consistent with the ΛCDM predictions from More et al. (2015) and Diemer (2020a), and Eq. (45) is itself derived from those same simulations.

As reported in Table 2 and detailed in Appendix D, the w_{cg} modelling yields robust constraints on the DK14 infalling term parameters, namely b_e and s_e, while weak-lensing observations do not probe this region. This is not attributable to different measurement precisions, which are similar for the two probes, but to the fact that w_{cg} is more directly sensitive to the spatial matter distribution in the infall region. Weak lensing, instead, probes $\Delta\Sigma_t$, an enclosed-mass quantity that is less sensitive to the detailed structure of the infalling region. Further discussions on the constraints on DK14 parameters can be found in Appendix D. In agreement with L25, we find that the f_{off} posterior aligns with the prior and $\sigma_{off} = 0.21 \pm 0.11\ h^{-1}$Mpc. The latter constraint

agrees also with literature simulation and observational results (Saro et al. 2015; Zhang et al. 2019; Yan et al. 2020; Seppi et al. 2023; Sommer et al. 2024). As shown in Table 2, we constrain the average galaxy bias parameters in Eq. (29) through the w_{cg} modelling, obtaining $b_{g,0} = 1.17^{+0.18}_{-0.17}$, $b_{g,\lambda^*} = -0.10^{+0.11}_{-0.11}$, and $b_{g,z} = 0.31^{+0.35}_{-0.33}$. A positive redshift evolution of $\langle b_g \rangle$ is expected, because galaxies at higher redshifts reside in rarer, more biased haloes. Our analysis, however, does not yield a significant redshift trend, as $b_{g,z}$ is consistent with zero within 1σ. Similarly, we find no significant dependence on λ^*. Future, more precise w_{cg} measurements will allow for a more detailed modelling of the galaxy bias.

6. Discussion and conclusions

In this paper, we presented an analysis of the splashback radius for the richest 8730 optically-selected galaxy clusters from the AMICO KiDS-1000 catalogue (Maturi et al. 2025). The sample covers an effective area of 839 deg^2 and spans the redshift range $z \in [0.1, 0.8]$. We measured and modelled the reduced tangential shear, g_t, and the cluster-galaxy projected correlation function, w_{cg}, of cluster ensembles, binning in redshift and mass proxy. Our modelling strategy, based on the techniques employed in recent cosmological analyses, allowed us to reconstruct the average properties of the underlying dark matter halo population, such as the normalised splashback radius, $\mathcal{R}_{sp}$, the splashback radius, r_{sp}, and the mass accretion rate, Γ.

Our constraints confirm the results of ΛCDM simulations and agree with observational studies in the literature. The r_{sp} estimates from g_t and w_{cg} agree within 1σ, though w_{cg} yields slightly lower values. This small offset may reflect a mild dynamical friction effect on satellite galaxies. We caution that galaxy selection is expected to play a role, as dynamical friction preferentially affects the most massive cluster members. Furthermore, the precision of our r_{sp} estimates is among the best available in the literature to date. It amounts to 14% in the case of g_t modelling, while w_{cg} constraints have a precision 10%. The measurements of w_{cg} also uniquely constrain the profile of the infalling material, which is not probed by weak-lensing observations.

A natural question is whether g_t and w_{cg} estimates of r_{sp} should be combined into a single constraint. We have chosen not to do so because the two probes are physically distinct: g_t traces the total matter distribution, whereas w_{cg} is sensitive to cluster member galaxies, which are affected by dynamical friction. The observed difference between the two measurements is consistent with this expected bias. Combining them would therefore average a biased and an unbiased estimate of r_{sp}. Future analyses with more complete galaxy samples or explicit modelling of dynamical friction may allow for a joint r_{sp} constraint.

As discussed in Sect. 4.6, we assumed that the net effect of orientation and projections on the w_{cg} measurements is absorbed by the free galaxy bias. The impact of this assumption on w_{cg} will be tested in future studies based on simulations. Intrinsic alignments are expected to have a negligible impact in our analysis, contributing only a sub-percent systematic error to cluster profiles (Chisari et al. 2014; Sereno et al. 2018). In the modelling of g_t, L25 demonstrated that anisotropic boosts, affecting the correlation functions on large scales due to optical projection effects (Sunayama et al. 2020; Wu et al. 2022; Sunayama 2023; Park et al. 2023; Zhou et al. 2024; Nyarko Nde et al. 2025), have negligible impact on our mass constraints. In particular, L25 adopted a model designed for cluster samples se-

lected with the red-sequence Matched-filter Probabilistic Percolation (redMaPPer, Rykoff et al. 2014) algorithm. This approximation holds in the case of a cosmological two-halo term, which mildly depends on the free parameters considered in the analysis. In this work, the cosmological two-halo is replaced by a free infalling term (Eq. 10), whose shape is poorly constrained by weak-lensing observations. Thus, we do not expect a dramatic impact of the anisotropic boosts on the results from the g_t modelling. Nonetheless, the constraints obtained from w_{cg} measurements may be biased due to this selection effect. In the future we will effectively test the impact of this selection bias on r_{sp}, developing dedicated mock data sets that simulate AMICO detections. We will also test how the assumption of the Diemer (2025) model, adopted as an alternative to the DK14 profile (Eq. 8), affects our results. The Diemer (2025) model requires higher data quality because it includes a larger number of free parameters compared to DK14, and KiDS-Legacy data (Wright et al. 2024) can provide the statistical power needed to constrain these additional degrees of freedom. We also note that the DK14 model is extrapolated up to very large scales for the derivation of g_t (Eq. 16) and w_{cg} (Eq. 17) models. The impact of such extrapolation shall be assessed through simulations.

Based on simulations, Shin & Diemer (2023) demonstrated that the luminosity difference between the brightest cluster galaxy and its brightest satellites, known as magnitude gap, serves as a reliable tracer of both the mass accretion rate and r_{sp}. This gap widens as satellites undergo disruption and halo accretion slows, also representing an indicator of system age (Jones et al. 2003; Deason et al. 2013; Yang et al. 2025). Data from KiDS-Legacy and Stage-IV surveys, such as *Euclid* (Euclid Collaboration et al. 2025) and the *Vera C. Rubin Observatory* (*Rubin*/LSST, Ivezic et al. 2008), will allow us to empirically constrain the correlation between r_{sp} and the magnitude gap. Stage-IV data can potentially shed light also on the stellar splashback radius, traced by the intracluster light (Dacunha et al. 2025; Walker et al. 2025), and on eventual deviations from General Relativity probed by the outskirts of galaxy clusters (Contigiani et al. 2023; Butt et al. 2025). As discussed in Appendix C, r_{sp} estimates obtained assuming the Planck18 cosmology are systematically lower than those from the baseline analysis, though they remain consistent within 0.5σ. With future data, the reduction in statistical uncertainties will enhance the r_{sp} sensitivity to cosmological parameters. Lastly, while the present r_{sp} measurements from g_t and w_{cg} are consistent within 1σ, upcoming data may better constrain the role of dynamical friction on cluster galaxies.

References

Adelberger, K. L., Steidel, C. C., Pettini, M., et al. 2005, ApJ, 619, 697
Adhikari, S., Dalal, N., & Chamberlain, R. T. 2014, J. Cosm. Astro-Particle Phys., 2014, 019
Aihara, H., Allende Prieto, C., An, D., et al. 2011, ApJ Suppl., 193, 29
Alam, S., Albareti, F. D., Allende Prieto, C., et al. 2015, ApJ Suppl., 219, 12
Baltz, E. A., Marshall, P., & Oguri, M. 2009, J. Cosm. Astro-Particle Phys., 2009, 015
Bartelmann, M. & Schneider, P. 2001, Phys. Rept., 340, 291
Baxter, E., Chang, C., Jain, B., et al. 2017, ApJ, 841, 18
Bellagamba, F., Roncarelli, M., Maturi, M., & Moscardini, L. 2018, MNRAS, 473, 5221
Beltz-Mohrmann, G. D. & Berlind, A. A. 2021, ApJ, 921, 112
Benítez, N. 2000, ApJ, 536, 571
Bertschinger, E. 1985, ApJ Suppl., 58, 39
Bhattacharya, S., Habib, S., Heitmann, K., & Vikhlinin, A. 2013, ApJ, 766, 32
Bhattacharyya, J., Adhikari, S., Banerjee, A., et al. 2022, ApJ, 932, 30
Bianconi, M., Buscicchio, R., Smith, G. P., et al. 2021, ApJ, 911, 136
Blake, C., Amon, A., Childress, M., et al. 2016, MNRAS, 462, 4240
Bleem, L. E., Stalder, B., de Haan, T., et al. 2015, ApJ Suppl., 216, 27
Böhringer, H., Schuecker, P., Guzzo, L., et al. 2004, A&A, 425, 367
Bryan, G. L. & Norman, M. L. 1998, ApJ, 495, 80
Bulbul, E., Liu, A., Pasini, T., et al. 2022, A&A, 661, A10
Butt, M. A., Haridasu, S., Diaferio, A., et al. 2025, arXiv e-prints, arXiv:2504.16685
Capaccioli, M. & Schipani, P. 2011, The Messenger, 146, 2
Cardone, V. F., Karmakar, P., De Petris, M., & Maoli, R. 2021, Phys. Rev. D, 103, 064065
Chang, C., Baxter, E., Jain, B., et al. 2018, ApJ, 864, 83
Chisari, N. E., Mandelbaum, R., Strauss, M. A., Huff, E. M., & Bahcall, N. A. 2014, MNRAS, 445, 726
Contigiani, O., Hoekstra, H., & Bahé, Y. M. 2019, MNRAS, 485, 408
Contigiani, O., Hoekstra, H., Brouwer, M. M., et al. 2023, MNRAS, 518, 2640
Costanzi, M., Rozo, E., Simet, M., et al. 2019, MNRAS, 488, 4779
Coupon, J., Kilbinger, M., McCracken, H. J., et al. 2012, A&A, 542, A5
Covone, G., Sereno, M., Kilbinger, M., & Cardone, V. F. 2014, ApJ Lett., 784, L25
Dacunha, T., Mansfield, P., & Wechsler, R. 2025, arXiv e-prints, arXiv:2508.02837
Davis, M. & Peebles, P. J. E. 1983, ApJ, 267, 465
de Jong, J. T. A., Verdoes Kleijn, G. A., Erben, T., et al. 2017, A&A, 604, A134
Deason, A. J., Conroy, C., Wetzel, A. R., & Tinker, J. L. 2013, ApJ, 777, 154
Despali, G., Moscardini, L., Nelson, D., et al. 2025, A&A, 697, A213
Diemer, B. 2017, ApJ Suppl., 231, 5
Diemer, B. 2020a, ApJ Suppl., 251, 17
Diemer, B. 2020b, ApJ, 903, 87
Diemer, B. 2025, MNRAS, 536, 1718
Diemer, B. & Kravtsov, A. V. 2014, ApJ, 789, 1
Diemer, B. & Kravtsov, A. V. 2015, ApJ, 799, 108
Diemer, B., Mansfield, P., Kravtsov, A. V., & More, S. 2017, ApJ, 843, 140
Ding, J., Dalal, R., Sunayama, T., et al. 2025, MNRAS, 536, 572
Driver, S. P., Bellstedt, S., Robotham, A. S. G., et al. 2022, MNRAS, 513, 439
Driver, S. P., Hill, D. T., Kelvin, L. S., et al. 2011, MNRAS, 413, 971
Duffy, A. R., Schaye, J., Kay, S. T., & Dalla Vecchia, C. 2008, MNRAS, 390, L64
Eckert, D., Ettori, S., Robertson, A., et al. 2022, A&A, 666, A41
Edge, A., Sutherland, W., Kuijken, K., et al. 2013, The Messenger, 154, 32
Einasto, J. 1965, Trudy Astrofizicheskogo Instituta Alma-Ata, 5, 87
Eltvedt, A. M., Shanks, T., Metcalfe, N., et al. 2024, MNRAS, 535, 2092
Euclid Collaboration, Mellier, Y., Abdurro'uf, et al. 2025, A&A, 697, A1
Euclid Collaboration: Adam, R., Vannier, M., Maurogordato, S., et al. 2019, A&A, 627, A23
Fenech Conti, I., Herbonnet, R., Hoekstra, H., et al. 2017, MNRAS, 467, 1627
Fillmore, J. A. & Goldreich, P. 1984, ApJ, 281, 1
Fong, M. & Han, J. 2021, MNRAS, 503, 4250
Gao, L., Navarro, J. F., Cole, S., et al. 2008, MNRAS, 387, 536
García, R., Salazar, E., Rozo, E., et al. 2023, MNRAS, 521, 2464
Ghirardini, V., Bulbul, E., Artis, E., et al. 2024, A&A, 689, A298
Giblin, B., Heymans, C., Asgari, M., et al. 2021, A&A, 645, A105
Giocoli, C., Marulli, F., Moscardini, L., et al. 2021, A&A, 653, A19
Giocoli, C., Palmucci, L., Lesci, G. F., et al. 2024, A&A, 687, A79
Haggar, R., Amoura, Y., Mpetha, C. T., et al. 2024, ApJ, 972, 28
Hartlap, J., Simon, P., & Schneider, P. 2007, A&A, 464, 399

Henson, M. A., Barnes, D. J., Kay, S. T., McCarthy, I. G., & Schaye, J. 2017, MNRAS, 465, 3361

Hildebrandt, H., van den Busch, J. L., Wright, A. H., et al. 2021, A&A, 647, A124

Hilton, M., Hasselfield, M., Sifón, C., et al. 2018, ApJ Suppl., 235, 20

Hoekstra, H., Mahdavi, A., Babul, A., & Bildfell, C. 2012, MNRAS, 427, 1298

Ingoglia, L., Covone, G., Sereno, M., et al. 2022, MNRAS, 511, 1484

Ivezic, Z., Axelrod, T., Brandt, W. N., et al. 2008, Serbian Astronomical Journal, 176, 1

Johnston, D. E., Sheldon, E. S., Wechsler, R. H., et al. 2007, arXiv e-prints, arXiv:0709.1159

Jones, L. R., Ponman, T. J., Horton, A., et al. 2003, MNRAS, 343, 627

Joshi, J., Rana, D., More, S., & Klein, M. 2025, arXiv e-prints, arXiv:2506.08925

Kohonen, T. 1982, Biological Cybernetics, 43, 59

Kuijken, K. 2011, The Messenger, 146, 8

Kuijken, K., Heymans, C., Dvornik, A., et al. 2019, A&A, 625, A2

Landy, S. D. & Szalay, A. S. 1993, ApJ, 412, 64

Lee, B. E., Le Brun, A. M. C., Haq, M. E., et al. 2018, MNRAS, 479, 890

Lesci, G. F., Marulli, F., Moscardini, L., et al. 2025, A&A, 703, A25

Lewis, A. & Challinor, A. 2011, ascl:1102.026

Liske, J., Baldry, I. K., Driver, S. P., et al. 2015, MNRAS, 452, 2087

Marulli, F., Veropalumbo, A., García-Farieta, J. E., et al. 2021, ApJ, 920, 13

Marulli, F., Veropalumbo, A., & Moresco, M. 2016, Astronomy and Computing, 14, 35

Maturi, M., Bellagamba, F., Radovich, M., et al. 2019, MNRAS, 485, 498

Maturi, M., Radovich, M., Moscardini, L., et al. 2025, A&A, 701, A201

McClintock, T., Varga, T. N., Gruen, D., et al. 2019, MNRAS, 482, 1352

Miller, L., Kitching, T. D., Heymans, C., Heavens, A. F., & van Waerbeke, L. 2007, MNRAS, 382, 315

Mitchell, M. A., Arnold, C., & Li, B. 2021, MNRAS, 502, 6101

Miyazaki, S., Komiyama, Y., Nakaya, H., et al. 2012, in Society of Photo-Optical Instrumentation Engineers (SPIE) Conference Series, Vol. 8446, Ground-based and Airborne Instrumentation for Astronomy IV, ed. I. S. McLean, S. K. Ramsay, & H. Takami, 84460Z

More, S., Diemer, B., & Kravtsov, A. V. 2015, ApJ, 810, 36

More, S., Miyatake, H., Takada, M., et al. 2016, ApJ, 825, 39

Mpetha, C. T., Taylor, J. E., Amoura, Y., & Haggar, R. 2024, MNRAS, 532, 2521

Murata, R., Sunayama, T., Oguri, M., et al. 2020, Publ. Astron. Soc. Japan, 72, 64

Navarro, J. F., Frenk, C. S., & White, S. D. M. 1997, ApJ, 490, 493

Nyarko Nde, T., Wu, H.-Y., Cao, S., et al. 2025, arXiv e-prints, arXiv:2510.00753

Park, Y., Sunayama, T., Takada, M., et al. 2023, MNRAS, 518, 5171

Peter, A. H. G., Rocha, M., Bullock, J. S., & Kaplinghat, M. 2013, MNRAS, 430, 105

Pizzardo, M., Geller, M. J., Kenyon, S. J., & Damjanov, I. 2024, A&A, 683, A82

Pizzuti, L., Sartoris, B., Amendola, L., et al. 2017, J. Cosm. Astro-Particle Phys., 2017, 023

Planck Collaboration, Aghanim, N., Akrami, Y., et al. 2020, A&A, 641, A6

Planck Collaboration XXIV. 2016, A&A, 594, A24

Postman, M., Coe, D., Benítez, N., et al. 2012, ApJ Suppl., 199, 25

Rana, D., More, S., Miyatake, H., et al. 2023, MNRAS, 522, 4181

Robertson, A., Harvey, D., Massey, R., et al. 2019, MNRAS, 488, 3646

Roche, N. & Eales, S. A. 1999, MNRAS, 307, 703

Romanello, M., Marulli, F., Moscardini, L., et al. 2024, A&A, 682, A72

Rosselli, D., Marulli, F., Veropalumbo, A., Cimatti, A., & Moscardini, L. 2023, A&A, 669, A29

Rykoff, E. S., Rozo, E., Busha, M. T., et al. 2014, ApJ, 785, 104

Ryu, S. & Lee, J. 2021, ApJ, 917, 98

Ryu, S. & Lee, J. 2022, ApJ, 933, 189

Salazar, E. M., Rozo, E., García, R., et al. 2025, Phys. Rev. D, 111, 043527

Saro, A., Bocquet, S., Rozo, E., et al. 2015, MNRAS, 454, 2305

Schaller, M., Frenk, C. S., Bower, R. G., et al. 2015, MNRAS, 451, 1247

Schneider, P. & Seitz, C. 1995, A&A, 294, 411

Seitz, C. & Schneider, P. 1997, A&A, 318, 687

Seppi, R., Comparat, J., Ghirardini, V., et al. 2024, A&A, 686, A196

Seppi, R., Comparat, J., Nandra, K., et al. 2023, A&A, 671, A57

Sereno, M. & Ettori, M. 2015a, MNRAS, 450, 3675

Sereno, M. & Ettori, S. 2015b, MNRAS, 450, 3633

Sereno, M., Giocoli, C., Izzo, L., et al. 2018, Nature Astronomy, 2, 744

Shao, M. & Anbajagane, D. 2024, The Open Journal of Astrophysics, 7, 29

Sheldon, E. S., Johnston, D. E., Frieman, J. A., et al. 2004, Astron. J., 127, 2544

Shin, T., Adhikari, S., Baxter, E. J., et al. 2019, MNRAS, 487, 2900

Shin, T., Jain, B., Adhikari, S., et al. 2021, MNRAS, 507, 5758

Shin, T.-h. & Diemer, B. 2023, MNRAS, 521, 5570

Sommer, M. W., Schrabback, T., Ragagnin, A., & Rockenfeller, R. 2024, MNRAS, 532, 3359

Sun, X., O'Neil, S., Shen, X., & Vogelsberger, M. 2025, arXiv e-prints, arXiv:2503.04882

Sunayama, T. 2023, MNRAS, 521, 5064

Sunayama, T., Park, Y., Takada, M., et al. 2020, MNRAS, 496, 4468

Sutherland, W., Emerson, J., Dalton, G., et al. 2015, A&A, 575, A25

The Dark Energy Survey Collaboration. 2005, arXiv e-prints, astro

Tinker, J., Kravtsov, A. V., Klypin, A., et al. 2008, ApJ, 688, 709

Tinker, J. L., Weinberg, D. H., Zheng, Z., & Zehavi, I. 2005, ApJ, 631, 41

Umetsu, K. & Diemer, B. 2017, ApJ, 836, 231

van den Busch, J. L., Hildebrandt, H., Wright, A. H., et al. 2020, A&A, 642, A200

van den Busch, J. L., Wright, A. H., Hildebrandt, H., et al. 2022, A&A, 664, A170

Viola, M., Cacciato, M., Brouwer, M., et al. 2015, MNRAS, 452, 3529

Vladimir, Z., Osinga, C., Diemer, B., Salazar, E. M., & Rozo, E. 2025, arXiv e-prints, arXiv:2506.09146

Voges, W., Aschenbach, B., Boller, T., et al. 1999, A&A, 349, 389

Walker, K., Ludlow, A., Power, C., Knebe, A., & Cui, W. 2025, arXiv e-prints, arXiv:2508.07232

Wehrens, R. & Buydens, L. M. C. 2007, Journal of Statistical Software, 21, 1

Wehrens, R. & Kruisselbrink, J. 2018, Journal of Statistical Software, 87, 1

Wright, A. H., Hildebrandt, H., van den Busch, J. L., & Heymans, C. 2020, A&A, 637, A100

Wright, A. H., Kuijken, K., Hildebrandt, H., et al. 2024, A&A, 686, A170

Wu, H.-Y., Costanzi, M., To, C.-H., et al. 2022, MNRAS, 515, 4471

Yan, Z., Raza, N., Van Waerbeke, L., et al. 2020, MNRAS, 493, 1120

Yang, M., Han, J., Wang, W., et al. 2025, arXiv e-prints, arXiv:2508.00667

Yang, X., Mo, H. J., van den Bosch, F. C., et al. 2006, MNRAS, 373, 1159

Yu, Q. S., O'Neil, S., Shen, X., et al. 2025, arXiv e-prints, arXiv:2507.22102

Zhang, Y., Jeltema, T., Hollowood, D. L., et al. 2019, MNRAS, 487, 2578

Zhou, C., Wu, H.-Y., Salcedo, A. N., et al. 2024, Phys. Rev. D, 110, 103508

Zhou, Y. & Han, J. 2023, MNRAS, 525, 2489

Zürcher, D. & More, S. 2019, ApJ, 874, 184

Appendix A: Halo miscentring model

To model the contribution due to the miscentred population of clusters, we assumed that the probability of a lens being at a projected distance R_s from the chosen centre, namely $P(R_s)$, follows a Rayleigh distribution (following, e.g. Johnston et al. 2007; Viola et al. 2015), that is

$$P(R_s) = \frac{R_s}{\sigma_{off}^2} \exp\left[-\frac{1}{2}\left(\frac{R_s}{\sigma_{off}}\right)^2\right], \tag{A.1}$$

where σ_{off} is the standard deviation of the halo misplacement distribution on the plane of the sky, expressed in units of h^{-1}Mpc. The corresponding azimuthally averaged profile is given by (Yang et al. 2006)

$$\Sigma(R|R_s) = \frac{1}{2\pi}\int_0^{2\pi} \Sigma_{cen}\left(\sqrt{R^2 + R_s^2 - 2RR_s\cos\theta}\right)d\theta, \tag{A.2}$$

where Σ_{cen} is the centred surface mass density, while θ is the polar angle in the plane of the sky. The surface mass density distribution of a miscentred halo is expressed as

$$\Sigma_{off}(R) = \int P(R_s)\,\Sigma(R|R_s)\,dR_s. \tag{A.3}$$

Analogously to Eq. (12), the miscentred tangential reduced shear, $g_{t,off}$, has the following expression:

$$g_{t,off}(R, M, z) = \frac{\Delta\Sigma_{t,off}(R, M, z)\,\langle\Sigma_{crit}^{-1}(z)\rangle}{1 - \Sigma_{off}(R, M, z)\,\langle\Sigma_{crit}^{-1}(z)\rangle^{-1}\,\langle\Sigma_{crit}^{-2}(z)\rangle}, \tag{A.4}$$

where Σ_{off} is given by Eq. (A.3), while $\Delta\Sigma_{t,off}$ is derived by replacing Σ with Σ_{off} in Eq. (14).

Appendix B: Cluster-galaxy correlation model

The 3D halo-matter correlation function, $\xi_{hm}(\boldsymbol{r})$, is defined as follows

$$\xi_{hm}(\boldsymbol{r}) \equiv \langle\delta_h(\boldsymbol{x})\,\delta_m(\boldsymbol{x}+\boldsymbol{r})\rangle_{\boldsymbol{x}}, \tag{B.1}$$

where $\boldsymbol{x}$ denotes the 3D comoving position of a halo centre, δ_h and δ_m are the halo and matter overdensity fields, respectively, while $\langle\ldots\rangle_{\boldsymbol{x}}$ represents the average over halo positions. The matter density field is defined as

$$\delta_m(\boldsymbol{x}) \equiv \frac{\rho(\boldsymbol{x}) - \rho_m}{\rho_m}, \tag{B.2}$$

where ρ is the local 3D matter density field and ρ_m is the mean matter density of the Universe. Because the right-hand side of Eq. (B.1) involves an average over halo centres, it can be expressed in terms of the conditional matter density profile around haloes, $\rho(\boldsymbol{r}|\boldsymbol{x})$:

$$\xi_{hm}(\boldsymbol{r}) = \frac{\langle\rho(\boldsymbol{r}|\boldsymbol{x}) - \rho_m\rangle_{\boldsymbol{x}}}{\rho_m} = \frac{\langle\Delta\rho(\boldsymbol{r}|\boldsymbol{x})\rangle_{\boldsymbol{x}}}{\rho_m}. \tag{B.3}$$

Here, $\langle\Delta\rho\rangle$ can be expressed as the DK14 profile in Eq. (8). Assuming spatial isotropy, the correlation function depends only on the separation $r = |\boldsymbol{r}|$. Furthermore, assuming that $\delta_c = \delta_h$, where δ_c is the galaxy cluster density field, we can express the 3D cluster-matter correlation function as

$$\xi_{cm}(r) = \frac{\Delta\rho(r)}{\rho_m}, \tag{B.4}$$

where we write $\langle\Delta\rho(r|x)\rangle_x$ as $\Delta\rho(r)$ for brevity. If galaxies are taken as biased tracers of the matter field, with galaxy overdensity $\delta_g \equiv b_g\delta_m$ and galaxy bias b_g, the corresponding cluster-galaxy correlation function follows from Eqs. (B.2) – (B.4):

$$\xi_{cg}(r) = b_g\frac{\Delta\rho(r)}{\rho_m}. \tag{B.5}$$

Here, b_g generally depends on the scale r. However, as discussed below, we assumed a constant galaxy bias. The cluster-galaxy correlation function projected over the line of sight, w_{cg}, is expressed as follows:

$$w_{cg}(R) = \int_0^\infty d\chi\,\tilde{n}(\chi)\,\xi_{cg}\left(\sqrt{R^2 + (\chi - \chi_c)^2}\right), \tag{B.6}$$

where R is the projected comoving distance from the cluster centre, $\tilde{n}(\chi)$ is the probability density function of galaxy comoving distances, and χ_c is the comoving distance of the cluster. We remark that χ and χ_c are comoving distances along the line of sight. Alternatively, Eq. B.6 can be integrated over the galaxy redshift, z_g:

$$w_{cg}(R) = \int_0^\infty dz_g\,n(z_g)\,\xi_{cg}\left(\sqrt{R^2 + [\chi(z_g) - \chi_c]^2}\right), \tag{B.7}$$

where $n(z_g)$ is the galaxy redshift probability density function. In Eq. (B.7), the Jacobian arising from the change of variable is absorbed into the definition of $n(z_g)$, namely

$$n(z_g) \equiv \tilde{n}(\chi(z_g))\frac{d\chi}{dz_g}. \tag{B.8}$$

Substituting Eq. (B.5) into Eq. (B.7), we obtain

$$w_{cg}(R) = \frac{\langle b_g\rangle}{\rho_m}\int_0^\infty dz_g\,n(z_g)\,\Delta\rho\left(\sqrt{R^2 + [\chi(z_g) - \chi_c]^2}\right), \tag{B.9}$$

where $\langle b_g\rangle$ is the galaxy bias averaged along the line of sight. With this approximation, we assume that b_g varies slowly along the line of sight, and that b_g does not depend on the projected separation R. These assumptions are motivated by the limited constraining power of our data on b_g.

Throughout this section, we assumed that $\boldsymbol{x}$, $\boldsymbol{r}$, and R are comoving distances. Conversely, in our analysis we measured and modelled w_{cg} as a function of the physical projected separation from cluster centres. In this case, Eq. (B.9) takes the following form:

$$w_{cg}(R, z) = \frac{\langle b_g(z)\rangle}{\rho_m(z)}\int_0^\infty dz_g\,n(z_g)\,\Delta\rho\left(\sqrt{R^2 + \left[\frac{\chi(z_g) - \chi_c}{1+z}\right]^2}, z\right), \tag{B.10}$$

where z is the cluster redshift. The $(1 + z)$ factor in the denominator accounts for the conversion from comoving to physical line-of-sight separation between the cluster and galaxies at the epoch of the cluster.

Appendix C: Robustness of the results

In this work, parameters that cannot be fully constrained by our data are fixed using simulations and previous observational results, as described in Sect. 4.6. Moreover, our sample selections are driven exclusively by the quality of the fit. For instance, we exclude clusters at $z > 0.8$ since their inclusion would otherwise
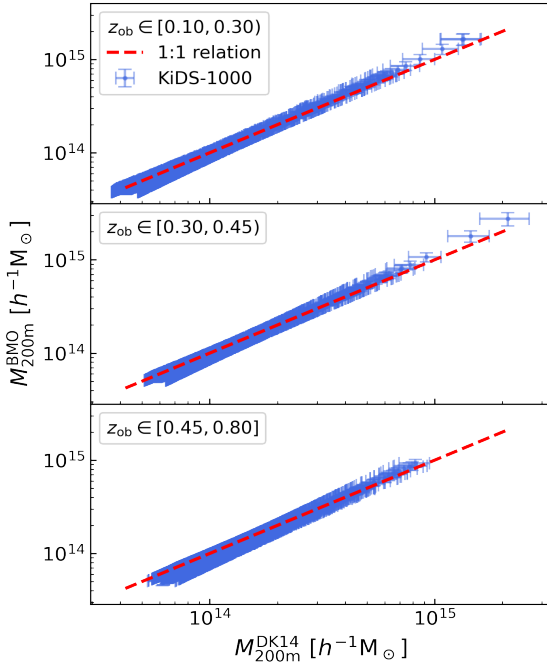
Fig. C.1. Comparison between M_{200}^{BMO}, derived by L25, and the mass estimates obtained from the g_t modelling presented in this work, M_{200}^{DK14}, for $z_{ob} \in [0.1, 0.3)$ (top), $z_{ob} \in [0.3, 0.45)$ (middle), and $z_{ob} \in [0.45, 0.8]$ (bottom), applying the λ^* cuts listed in Table 1 to the AMICO KiDS-1000 cluster sample. The mean and error bars are derived by marginalising the mass estimates over all the free model parameter posteriors. The dashed red lines represent the 1:1 relation.
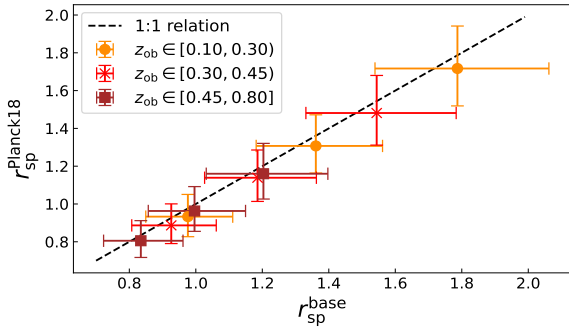

Fig. C.2. Splashback radius derived from the g_t modelling assuming Planck18 cosmology, $r_{sp}^{Planck18}$, compared to the one derived by assuming the cosmological parameters by L25, r_{sp}^{base}, for $z_{ob} \in [0.1, 0.3)$ (orange dots), $z_{ob} \in [0.3, 0.45)$ (red crosses), and $z_{ob} \in [0.45, 0.8]$ (brown squares).

reduce the fit accuracy. In this section, we assess the impact of these assumptions on our final results.

Several tests were already performed in L25, who carried out the weak-lensing mass calibration of the cluster sample analysed in this paper. They showed that weak-lensing measurements pass null tests, further demonstrating that the final mass constraints are robust against the choice of priors on the halo miscentring parameters. The same analysis also confirmed that our data lack the precision to detect any potential mass dependence of σ_{intr}. In addition, L25 demonstrated that fixing the mass slope of the $\log c_{200m} - \log M_{200m}$ relation (Eq. 32), denoted as c_M and discussed in Sect. 4.6, does not introduce any biases in the mass estimates. The same holds for the intrinsic scatter in the $\log c_{200m} - \log M_{200m}$ relation, which amounts to about 35%
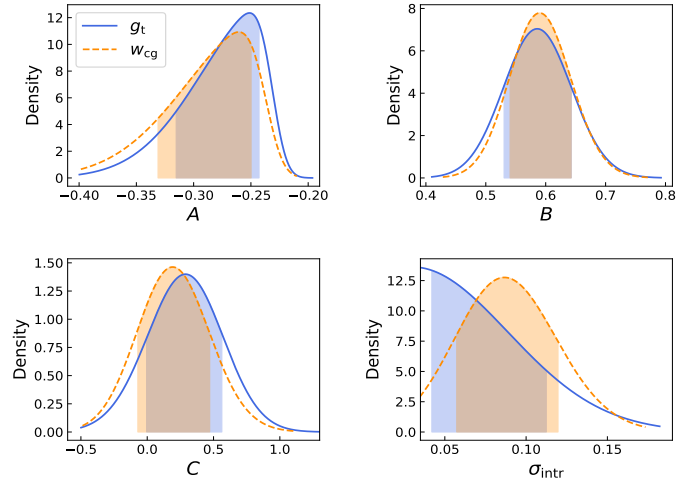
Fig. C.3. Posterior distributions of the $\log \lambda^* - \log M_{200m}$ relation parameters (Eq. 25) from the modelling of g_t (blue solid lines) and w_{cg} (orange dashed lines). Shaded areas represent 68% confidence regions.
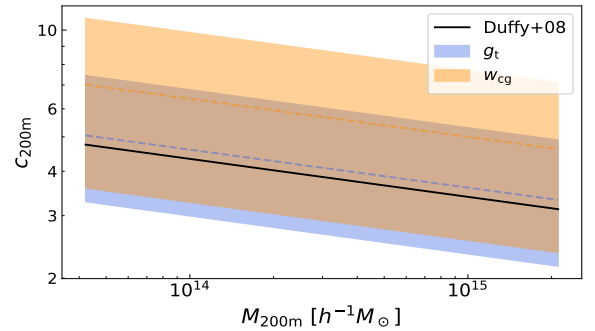

Fig. C.4. $\log c_{200m} - \log M_{200}$ relation constrained by g_t (blue band) and w_{cg} (orange band) measurements. The width of the bands represents the 68% confidence of the models, while the dashed lines display median values. The black solid line shows the model by Duffy et al. (2008). The cluster redshift assumed in this figure is $z = 0.45$.

(see e.g. Duffy et al. 2008; Bhattacharya et al. 2013; Diemer & Kravtsov 2015). Given our data set, this scatter is negligible compared to the statistical uncertainty on the amplitude of the relation, $\log c_0$.

Figure C.1 displays the comparison between the individual cluster mass estimates derived from the g_t modelling presented in this work (based on Eq. 54 in L25) and those from L25. Despite L25 adopting the truncated NFW profile by Baltz, Marshall, & Oguri (2009, BMO) rather than the DK14 profile in Eq. (8), and modelling the g_t profiles only up to 3.5 h^{-1}Mpc, we find excellent agreement.

As discussed in Sect. 5, in our analysis we assumed the median cosmological parameter values constrained by L25. To test the impact of this choice, we fixed the cosmological parameters to the median values from Planck18. The resulting splashback radius estimates obtained from the g_t modelling are systematically lower but consistent within 0.5σ (Fig. C.2). These lower r_{sp} estimates are expected, as the Ω_m value from Planck18, $\Omega_m = 0.31$, is larger than the one assumed in our baseline analysis, analysis, namely $\Omega_m = 0.22$. Indeed, larger Ω_m implies faster accretion rates and smaller r_{sp} (Diemer et al. 2017; Haggar et al. 2024; Mpetha et al. 2024). We verified that the same level of agreement holds for $\mathcal{R}_{sp}$. While this test was performed only for g_t modelling, we expect similar results for w_{cg}.
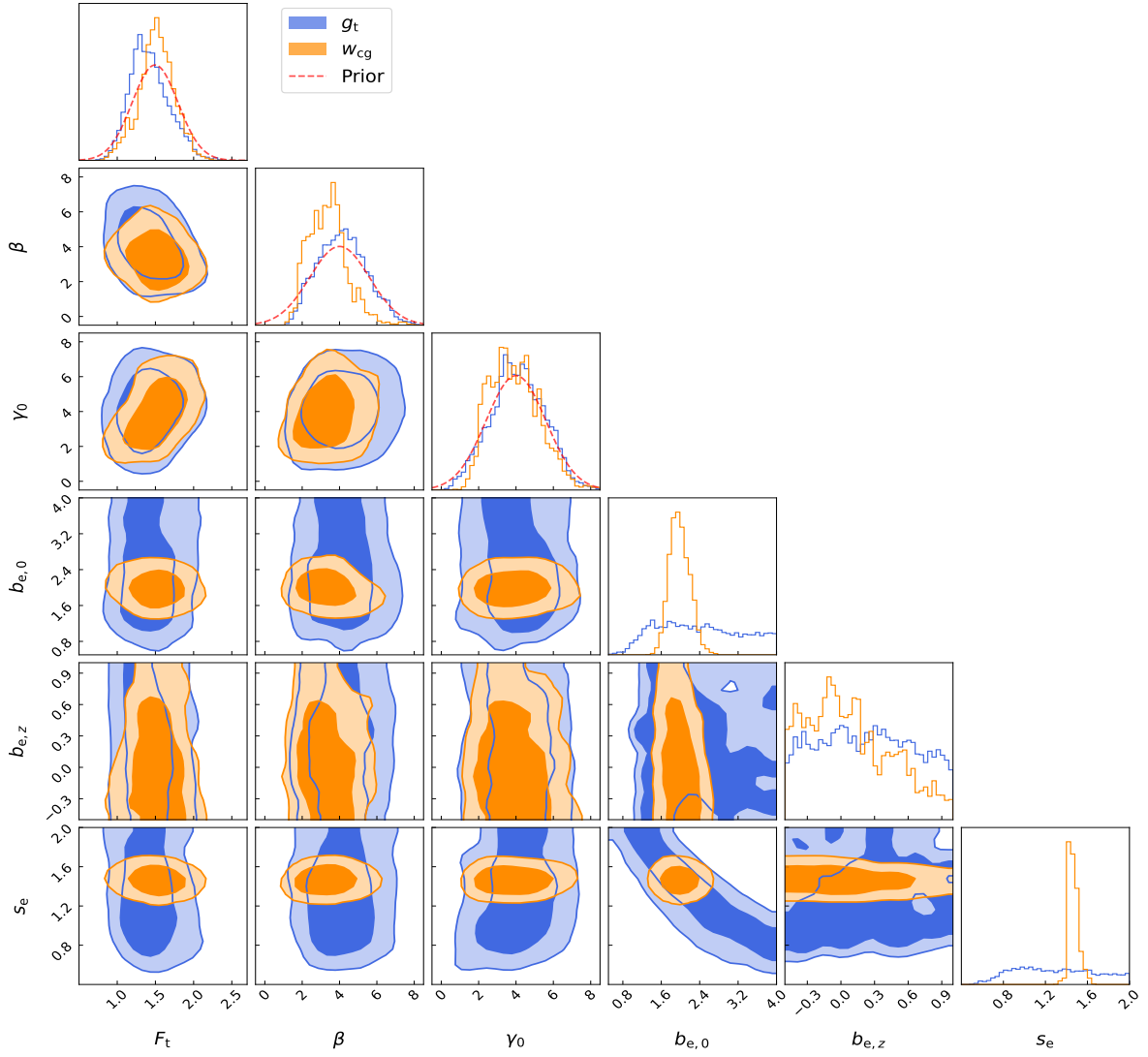
Fig. C.5. Constraints on the parameters of the transition factor and infalling term of the DK14 profile. The 68% and 84% confidence levels of the 2-dimensional posteriors from g_t (blue) and w_{cg} (orange) modellings are shown. The Gaussian priors on F_t, β, and γ_0 are represented by the red dashed lines.

Appendix D: Constraints on the DK14 parameters

In this work, we first estimated the parameters of the $\log \lambda^* - \log M_{200m}$ relation (Eq. 25) by modelling g_t, subsequently using the resulting posteriors as priors for the w_{cg} modelling. Figure C.3 shows that the two probes yield similar constraints on these parameters. The most significant differences appear in the posteriors for the amplitude, A, and the intrinsic scatter, σ_{intr}. For w_{cg}, the A posterior is shifted to lower values and is more heavily tailed, while σ_{intr} peaks at a larger value compared to the constraint from g_t. The σ_{intr} result can be explained by our assumption of $M_{200m} \equiv M_{g_t} \equiv M_{w_{cg}}$, where M_{g_t} and $M_{w_{cg}}$ are the weak-lensing and cluster-galaxy correlation function masses, respectively. In fact, these are scattered proxies of the true M_{200m} (see, e.g. Sereno & Ettori 2015b), with a larger scatter expected for $M_{w_{cg}}$ due to the large variance in cluster member galaxy distributions. The differences in A and σ_{intr} explain the larger statistical uncertainties on $M_{w_{cg}}$ compared to M_{g_t} (Fig. 4).

Figure C.4 shows that our constraints on the $\log c_{200m} - \log M_{200m}$ relation agree within 1σ with the model by Duffy et al. (2008). The r_{sp} results presented in Sect. 5 suggest that dynamical friction on cluster member galaxies imprints a splashback

feature in w_{cg} at smaller scales than in weak-lensing observations. Consequently, haloes traced by cluster galaxies should appear more concentrated. However, the large uncertainty on c_{200m} derived from w_{cg} (Fig. C.4) precludes any stronger conclusion on this point.

Figure C.5 shows that the constraints on the parameters of the DK14 transition factor (Eq. 9), namely F_t, β, and γ_0, align with the adopted Gaussian priors. The largest difference between prior and posterior occurs for β in the w_{cg} modelling, where the posterior median shifts from the prior by 0.5σ (see also Table 2). Furthermore, in this work we adopted uninformative priors on the infalling profile parameters in Eq. (10), namely b_e and s_e, allowing b_e to evolve with redshift (Eq. 11). As shown in Fig. C.5 and reported in Table 2, g_t measurements do not constrain these parameters, whereas w_{cg} provides strong constraints with a precision of 11% on $b_{e,0}$ and of 4% on s_e. Our resulting values, $b_{e,0} = 1.97^{+0.23}_{-0.19}$ and $s_e = 1.461^{+0.052}_{-0.046}$, also agree within 1σ with the theoretical predictions from DK14. Neither probe constrains the redshift evolution of b_e.